Role of medium heterogeneity and viscosity contrast in miscible flow regimes and mixing zone growth: A computational pore-scale approach

Saied Afshari, S. Hossein Hejazi,* and Apostolos Kantzas
Department of Chemical and Petroleum Engineering, University of Calgary, Calgary, Alberta, Canada, T2N1N4

(Received 12 January 2017; published 8 May 2018)

Miscible displacement of fluids in porous media is often characterized by the scaling of the mixing zone length with displacement time. Depending on the viscosity contrast of fluids, the scaling law varies between the square root relationship, a sign for dispersive transport regime during stable displacement, and the linear relationship, which represents the viscous fingering regime during an unstable displacement. The presence of heterogeneities in a porous medium significantly affects the scaling behavior of the mixing length as it interacts with the viscosity contrast to control the mixing of fluids in the pore space. In this study, the dynamics of the flow and transport during both unit and adverse viscosity ratio miscible displacements are investigated in heterogeneous packings of circular grains using pore-scale numerical simulations. The pore-scale heterogeneity level is characterized by the variations of the grain diameter and velocity field. The growth of mixing length is employed to identify the nature of the miscible transport regime at different viscosity ratios and heterogeneity levels. It is shown that as the viscosity ratio increases to higher adverse values, the scaling law of mixing length gradually shifts from dispersive to fingering nature up to a certain viscosity ratio and remains almost the same afterwards. In heterogeneous media, the mixing length scaling law is observed to be generally governed by the variations of the velocity field rather than the grain size. Furthermore, the normalization of mixing length temporal plots with respect to the governing parameters of viscosity ratio, heterogeneity, medium length, and medium aspect ratio is performed. The results indicate that mixing length scales exponentially with log-viscosity ratio and grain size standard deviation while the impact of aspect ratio is insignificant. For stable flows, mixing length scales with the square root of medium length, whereas it changes linearly with length during unstable flows. This scaling procedure allows us to describe the temporal variation of mixing length using a generalized curve for various combinations of the flow conditions and porous medium properties.

DOI: 10.1103/PhysRevFluids.3.054501

I. INTRODUCTION

Miscible displacement and mixing of fluids in heterogeneous porous media are of practical importance in many scientific and engineering applications including groundwater remediation [1–5], carbon dioxide sequestration [6], and enhanced oil recovery [7–9]. In a miscible displacement, fluid mixing results from molecular diffusion and mechanical dispersion in the microscopic scale and occurs over a transition zone called the mixing zone. Molecular diffusion occurs due to the existence of a concentration gradient, while mechanical dispersion arises from the variations in magnitude and direction of the local velocity. Any other mechanism that increases the fluids contact area also improves mixing. The size of the mixing zone measured along the general direction of displacement is usually characterized by a mixing length (denoted as L_M hereafter) which has been traditionally

*Corresponding author: shhejazi@ucalgary.ca

utilized to describe the level of fluid mixing [10–20]. The concept of mixing length first theoretically developed for flow in capillary tubes [21,22] and later extended to porous media [10,20]. The rate of mixing and consequently the magnitude of L_M strongly depends on the viscosity contrast of fluids and the heterogeneity of pore space [2]. When there is an unfavorable viscosity ratio, i.e., displacing fluid is less viscous than the displaced fluid, hydrodynamic instabilities develop at the leading edge of concentration front. These instabilities result in fingering of the displacing fluid through the porous medium. The nonuniform distribution of shape and size of the pores and throats in a porous medium also results in some preferred paths for flow and gives rise to the channeling of the flow. Viscous-driven fingering and heterogeneity-induced channeling are the two significant sources of bypassing and uneven concentration fronts in miscible displacements [23]. Their relative effects on mixing dictates the transport regime at different flow velocities. The scaling of L_M with displacement time is an indicator of this transport regime [12,24]. If L_M grows with the square root of time ($L_M \sim t^{0.5}$), the mixing and transport is dominated by dispersion and the displacement is called dispersive. On the other hand, a linear growth of L_M with time ($L_M \sim t$) is an indicator of fingering-dominated flow [12].

Experimental [10,11,13,25–28] and numerical [19,28–30] studies of miscible displacement in macroscale homogeneous porous media have shown that the transport regime is dispersive and L_M scales with $t^{0.5}$ during stable (unit viscosity/mobility ratio) displacements. During unstable (adverse viscosity/mobility ratio) displacements, however, the nonlinear behavior of viscous fingering, which is controlled by the mechanisms of tip splitting, spreading, shielding, and merging of fingers [19], affects the growth of mixing length. Both laboratory experiments [13,25,26,28] and numerical simulations [12,29,30] of unstable displacement in homogeneous media have revealed a crossover from an initial dispersive growth of mixing length to the linear mixing zone growth at low viscosity ratios, while only linear growth has been observed for large viscosity ratios.

The presence of heterogeneities in a nonhomogeneous porous medium adds to the complexity of mixing length growth behavior. In macroscale, the heterogeneity of porous media is usually characterized by the variance and correlation length of the permeability field which describe the degree of variation and spatial correlation, respectively. Some of the previous numerical studies of miscible displacement in heterogeneous permeability fields [12,19,31,32] have concluded that the transport regime at the unit viscosity ratio is dispersive and L_M grows with $t^{0.5}$. However, other studies [23,33] suggested that this behavior is relevant as long as the permeability is uncorrelated or the variance of permeability is small. If both variance and correlating length are sufficiently large, a channeling regime is encountered and L_M growth is linear, although there is no viscous fingering [23,33]. In adverse viscosity ratio displacements, the interaction of viscous fingering and heterogeneity governs the flow behavior and transport regime. Simulations of unstable displacement in correlated heterogeneous permeability fields [18,34] have indicated that L_M grows linearly with time and an increase in the variance of permeability results in higher growth rate. For uncorrelated media, however, when permeability variance is large, dispersive damping is significant and mixing length grows with the square root of time [23]. In periodically heterogeneous permeability fields (i.e., layered media), the scaling of mixing length was observed to be dependent on the magnitude of the Péclet number [12,35]. If the Péclet number is less than a critical value, the combined effects of axial dispersion and transverse homogenization of the concentration result in a layering-dominated flow where no tip splitting of the fingers occurs and the L_M grows dispersively ($L_M \sim t^{0.5}$). At higher Péclet numbers, if the permeability variation is small L_M grows linearly with time ($L_M \sim t$). However, layering-induced channeling can overcome the tip-splitting mechanism when permeability variation is sufficiently large and therefore leads to the dispersive growth regime [12,35]. Later [17], a generalized curve for mixing length growth in layered permeability fields was proposed which identified four different transport regimes: an initial diffusive regime ($L_M \sim t^{0.5}$) followed by a channeling regime ($L_M \sim t$) and then the lateral dispersion and finally viscous fingering.

Despite the extensive research on miscible displacement in porous media at macroscale, there are still inconsistent interpretations about the transport regime and scaling of mixing length with time, especially in heterogeneous media. It is fairly understood that both heterogeneity-induced channeling and viscous-driven instability determine the growth behavior of mixing length. However,

it remains unclear how their interactions change the transport regime between the two extremes of dispersive ($L_M \sim t^{0.5}$) and fingering ($L_M \sim t$) behavior. Most previous studies focus on the continuum modeling of each mechanism, while much less work has been done on their combined effect on fluid mixing. Also, these studies usually were conducted in macroscale permeability fields with the assumption of validity of the continuum Darcy level description of the flow, which neglects the variability of heterogeneity in scales smaller than the size of the continuum gridblocks. In Darcy flow, subgridblock local velocity variations are represented by the dispersion coefficient, which is usually anisotropic and velocity dependent and needs to be characterized accurately or otherwise leads to inaccurate results.

In this study, we model the pore-level miscible displacement in heterogeneous media by solving the point equations of flow and mass transport on pore-scale models with different levels of heterogeneity. In order to investigate the effect of viscous fingering and medium heterogeneity on mixing length growth, numerical simulations of miscible displacement are performed at different viscosity ratios and flow velocities. This approach enables us to accurately account for the various mechanisms contributing to the growth of mixing length and eliminate the prerequisite description of dispersion coefficient and the validity assessment of Darcy flow. In what follows, we first present the governing equations, the porous media model, and the numerical approaches in Sec. II. Results on the dynamics of the mixing length growth and its scaling are presented in Secs. III and IV, respectively. Finally, Sec. V summarizes the main conclusions from the present study.

II. PROBLEM SETUP AND MATHEMATICAL MODEL

A. Governing equations

Continuity, Navier-Stokes, and convection-diffusion equations are simultaneously solved to model miscible displacement in pore scale using digital images of porous media. It is assumed that the displacements are horizontal and the solution mixing is ideal, so there is no volume change upon solution mixing. The conservation of mass can be described by the continuity equation as

$$\nabla \cdot (\mathbf{u}) = 0. \tag{1}$$

Velocity and pressure profiles in the pore space are evaluated by combining the continuity equation [Eq. (1)] and the incompressible Navier-Stokes equation in the absence of gravity:

$$\rho \frac{\partial \mathbf{u}}{\partial t} + \rho(\mathbf{u} \cdot \nabla)\mathbf{u} = -\nabla p + \nabla \cdot \{\mu[\nabla \mathbf{u} + (\nabla \mathbf{u})^{\mathrm{T}}]\}. \tag{2}$$

In the above equations, $\mathbf{u}$ is the pore velocity vector, p is the pressure, and ρ and μ are mixture density and viscosity, respectively. To find the spatiotemporal solute concentrations, we solve the convection-diffusion equation as

$$\frac{\partial c}{\partial t} + \mathbf{u} \cdot \nabla c = \nabla \cdot (D \nabla c). \tag{3}$$

In this equation, c denotes the concentration of solute and D is the mutual diffusion coefficient of the miscible solutions which is assumed to be constant in this study. Viscosity variation with concentration can be characterized by either an exponential [36] or a quarter-law mixing rule [37]. Here a quarter-law power mixing rule for viscosity is adopted in the simulations to estimate the mixture viscosity:

$$\mu = \left[\mu_1^{-0.25} + \frac{c - c_0}{c_{\mathrm{inj}} - c_0} \left(\mu_2^{-0.25} - \mu_1^{-0.25} \right) \right]^{-4}, \tag{4}$$

where μ_1 and μ_2 are the viscosities of displaced and displacing solutions, respectively, and c_{inj} denotes the solute concentration in the injected solution while c_0 is the initial concentration in the media, which is zero in our simulations. We use $\bar{d}$, v, $\bar{d}/v$, μ_2 and $v\mu_2/\bar{d}$ as the characteristic parameters of length, velocity, time, viscosity, and pressure, respectively, to make the governing

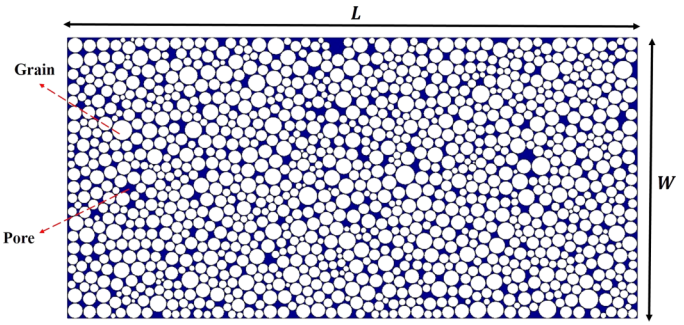

FIG. 1. Pore-scale representation of unconsolidated porous media.

equations dimensionless. Here $\bar{d}$ is the average grain diameter of the granular porous media (see Fig. 1) and v is the intrinsic velocity in the medium. The intrinsic velocity v is defined as v_{inj}/ϕ where v_{inj} is the injection velocity and ϕ is the porosity of medium. Using these characteristic parameters, the dimensionless governing equations are

$$\nabla \cdot (\mathbf{u}_{\text{D}}) = 0, \tag{5}$$

$$\frac{\partial \mathbf{u}_{\text{D}}}{\partial t_{\text{D}}} + (\mathbf{u}_{\text{D}} \cdot \nabla)\mathbf{u}_{\text{D}} = \frac{1}{\text{Re}}(-\nabla p_{\text{D}} + \nabla \cdot \{\mu_{\text{D}}[\nabla \mathbf{u}_{\text{D}} + (\nabla \mathbf{u}_{\text{D}})^{\text{T}}]\}), \tag{6}$$

$$\frac{\partial c_{\text{D}}}{\partial t_{\text{D}}} + \mathbf{u}_{\text{D}} \cdot \nabla c_{\text{D}} = \frac{1}{\text{Pe}} \nabla^2 c_{\text{D}}, \tag{7}$$

$$\mu_{\text{D}} = \left[\mu_{1,\text{D}}^{-0.25} + c_{\text{D}}\left(1 - \mu_{1,\text{D}}^{-0.25}\right)\right]^{-4}. \tag{8}$$

Here c_{D} is defined as $(c - c_0)/(c_{\text{inj}} - c_0)$, and Re and Pe are local (pore) Reynolds and Péclet numbers:

$$\text{Re} = \frac{\rho v \bar{d}}{\mu_2}, \tag{9}$$

$$\text{Pe} = \frac{v\bar{d}}{D}. \tag{10}$$

In subsurface flows, Reynolds number is low and the flow regime generally can be assumed to be laminar. The largest Reynolds number encountered in the simulations of this paper is about 0.2 (laminar flow condition). The pore-Péclet number is basically the ratio of the time it takes for diffusion to transport fluid particles over one grain diameter along the global flow direction to the time it takes for convection to do the same. In this work, Pe varies in the range 0.2–2000, which for the typical values of $10^{-10}\,\text{m}^2/\text{s}$ and 0.3 mm for D and $\bar{d}$, respectively, results in the intrinsic velocity to be in the range of 6.7×10^{-8} to $6.7 \times 10^{-4}\,\text{m/s}$. The value of $10^{-10}\,\text{m}^2/\text{s}$ for diffusion coefficient is a typical value for a hydrocarbon system [38], while an average grain size of 0.3 mm is a reasonable value for an unconsolidated granular medium [39,40]. We further define log-viscosity ratio (R) as the natural logarithm of the ratio of the in-place fluid viscosity (μ_1) to the injected fluid viscosity (μ_2):

$$R = \ln\left(\frac{\mu_1}{\mu_2}\right). \tag{11}$$

TABLE I. Patterns used in the simulations of this study and their properties.

Pattern name	$\bar{d}$ [mm]	CV	Length (L_D)	Aspect ratio ($A = L_D/W_D$)	Porosity
PM1	0.3	0	50	2	0.23
PM2	0.3	0.125	50	2	0.24
PM3	0.3	0.25	50	2	0.23
PM4	0.3	0.50	50	2	0.24
PM5	0.3	0.25	25	2	0.24
PM6	0.3	0.25	33.3	2	0.24
PM7	0.3	0.25	75	2	0.24
PM8	0.2	0.25	75	2	0.24
PM9	0.4	0.25	37.5	2	0.24
PM10	0.3	0.25	50	4	0.24
PM11	0.3	0.25	50	8	0.24

When R is greater than zero, the system is at adverse or unfavorable viscosity ratio, which usually ends in unstable flow and viscous fingering. A negative value of R indicates a favorable viscosity ratio, while a unit viscosity ratio is described by R equal to zero.

B. Porous media model

The pore-scale representation of heterogeneous porous media is achieved by constructing two-dimensional packings of circular disks. These circular disks in a packing can be considered as two-dimensional representation of sand grains in an unconsolidated sandpack with the dimensions of L_D and W_D ($[L_D, W_D] = [L, W]/\bar{d}$), and the aspect ratio of $A = L_D/W_D$ (Fig. 1). An in-house pattern generator is used to construct these packings based on the swelling grain reconstruction algorithm with variable grain diameters taken from a particle size distribution (PSD). The PSD defines the relative number of particles (grains) with a specific diameter in the packing [see Fig. 2(e)]. In this algorithm, a predefined number of points (representing the number of grains) are randomly distributed in the bulk medium with the coordinates of each point being the center of the final grain. Then, a radius is picked from the PSD and assigned to each point. Based on these radii, the points swell from zero radius to their assigned radius with a growth rate proportional to their assigned radius. At each swelling step, it is examined if the grains are overlapping, and this overlapping is eliminated by slightly shifting the center of the overlapped grains. This procedure is repeated until there is no overlapping, and then the next swelling step commences. At the final step, the radius of all grains is reduced by 2% in order the remove any contact between grains and provide the connectivity of the media. Using this method, several porous media with different levels of microscale (pore-scale) heterogeneity can be generated based on the PSD's standard deviation. The heterogeneity of these media is characterized by a coefficient of variation (CV) defined as

$$\mathrm{CV} = S_{d_D}, \tag{12}$$

where d_D is the dimensionless particle (grain) diameter ($d_D = d/\bar{d}$) and S_{d_D} describes the standard deviation of d_D [standard deviation of PSD, Fig. 2(e)]. This parameter is analogous to the standard deviation of permeability which is usually used to describe the heterogeneity in permeability fields [18,34].

Several pore-scale patterns are generated and used in the simulations. Table I summarizes the allocated names and geometrical properties of them. Figure 2 shows four of these patterns (PM1 to PM4) that have the same $\bar{d}$, A, and L_D, but different values of CV corresponding to the PSDs depicted in Fig. 2(e). Later they will be used to demonstrate how pore-scale heterogeneity affects the mixing length growth. In order to investigate the impact of medium length (L_D) on the growth of

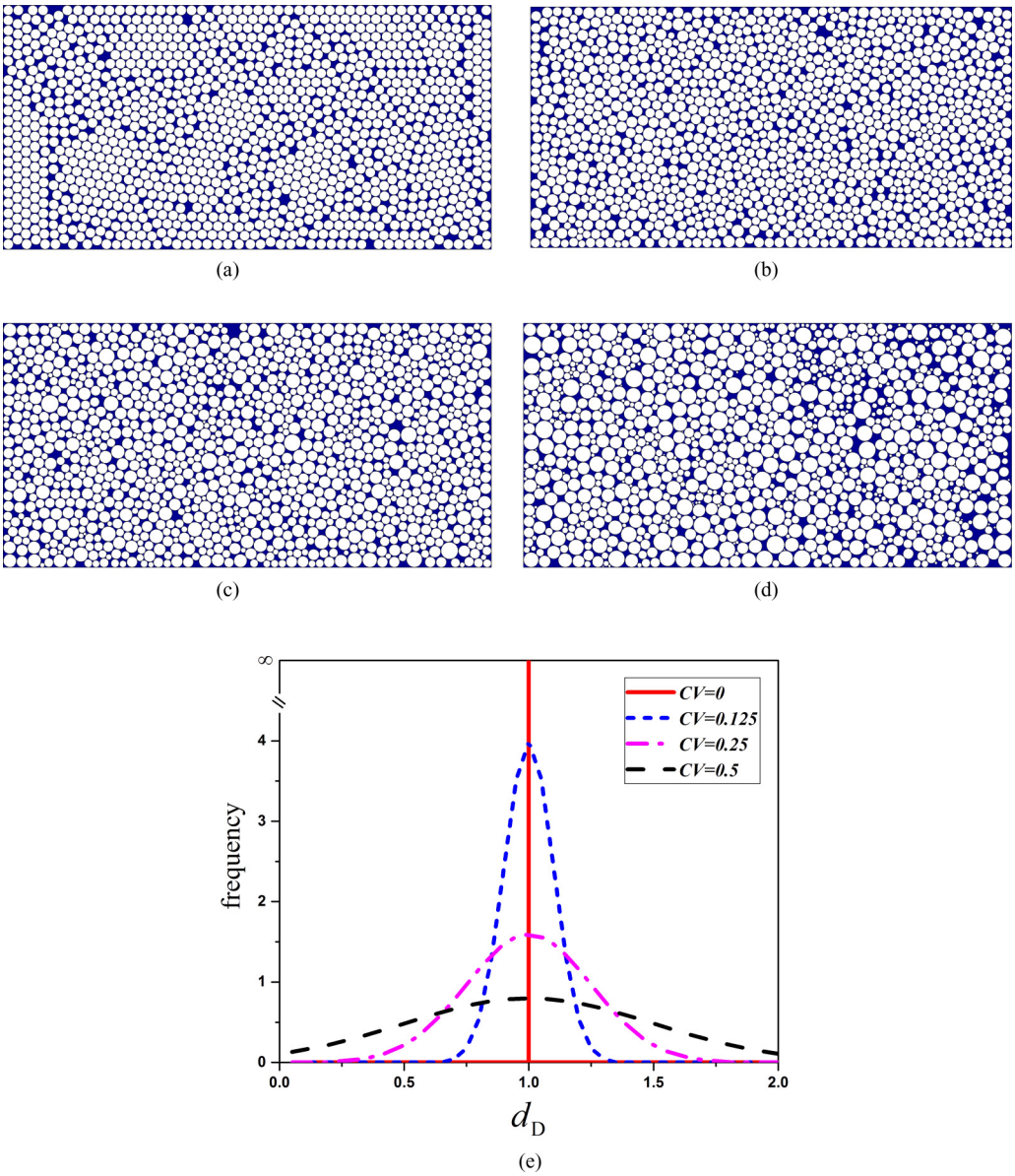

FIG. 2. Four patterns with $\bar{d} = 0.3$ mm, $L_D = 50$, $A = 2$, and different CV along with their corresponding PSDs. (a) PM1 with CV $= 0$, (b) PM2 with CV $= 0.125$, (c) PM3 with CV $= 0.25$, (d) PM4 with CV $= 0.5$, and (e) PSDs corresponding to different CV.

mixing zone, several patterns with different values of L_D are generated and used in the simulations (Fig. 3). The patterns PM3, PM5, PM6, and PM7 have the same $\bar{d}$, CV, and A, but different L_D, whereas PM8 and PM9 have different $\bar{d}$ compared to the others. Furthermore, to explore if the aspect ratio has any effect on the growth of mixing length, two other media, PM10 and PM11, with aspect ratios of 4 and 8, respectively, are constructed and compared to PM3, which has an aspect ratio of 2 (Fig. 4).

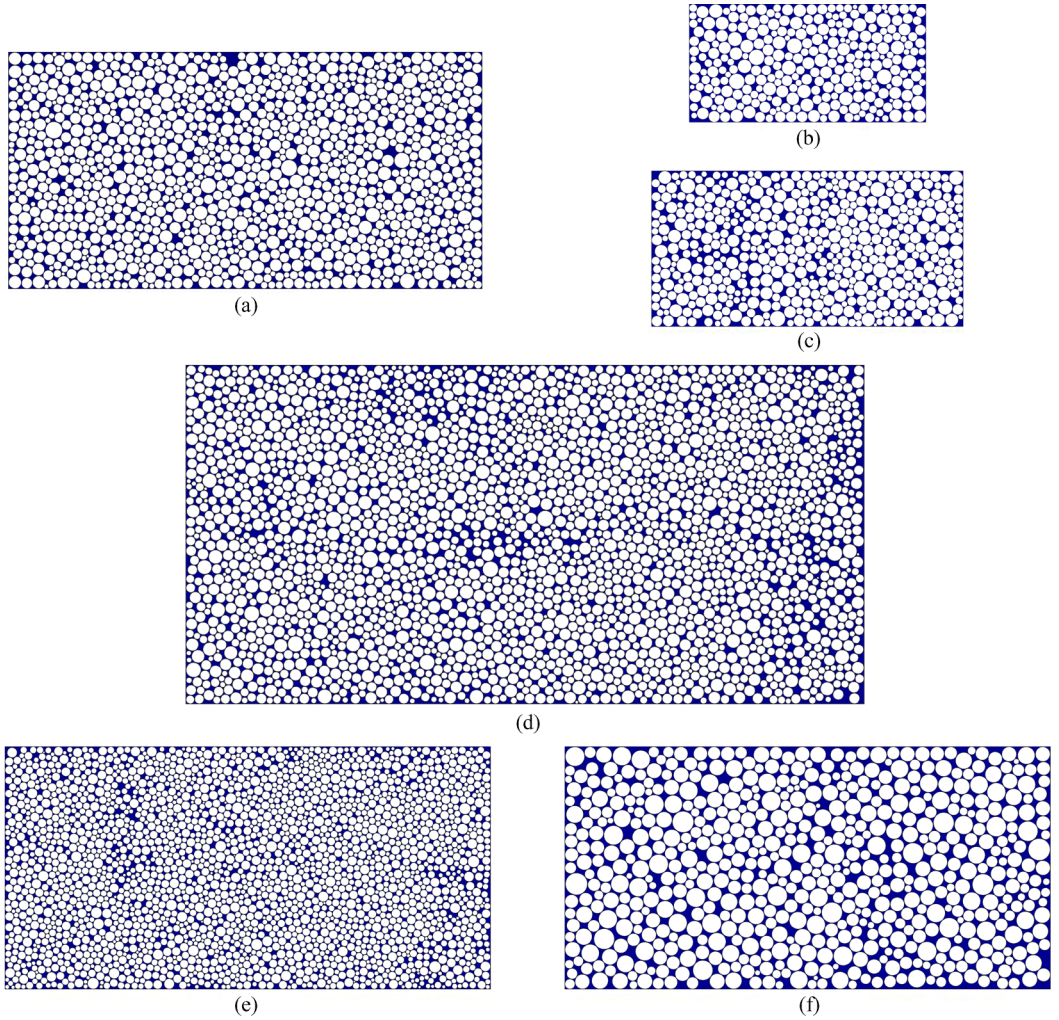

FIG. 3. Patterns with CV $= 0.25$, $A = 2$, and different L_{D} and/or $\bar{d}$. (a) PM3 with $L_{\mathrm{D}} = 50$ and $\bar{d} = 0.3$ mm, (b) PM5 with $L_{\mathrm{D}} = 25$ and $\bar{d} = 0.3$ mm, (c) PM6 with $L_{\mathrm{D}} = 33.3$ and $\bar{d} = 0.3$ mm, (d) PM7 with $L_{\mathrm{D}} = 75$ and $\bar{d} = 0.3$ mm, (e) PM8 with $L_{\mathrm{D}} = 75$ and $\bar{d} = 0.2$ mm, and (f) PM9 with $L_{\mathrm{D}} = 37.5$ and $\bar{d} = 0.4$ mm. Note that the patterns are depicted in the correct scales.

C. Numerical approach

Commercial code COMSOL [41] is used to solve Eqs. (5)–(8) using a full implicit finite-element scheme. To achieve this, the reconstructed images of porous media are discretized such that each pore is covered with several grid elements that are significantly smaller in size in comparison with the pore size. The initial and boundary conditions are set as illustrated in Fig. 5. The inlet condition for flow is constant injection velocity, while the outlet is constant atmospheric pressure ($p_{0,\mathrm{D}}$), which, in combination with incompressible flow assumption, guarantees the continuity of inlet and outlet fluxes. For mass transfer, constant concentration inflow and zero concentration gradient (Danckwerts boundary conditions) are imposed on the inlet and outlet boundaries, respectively. It is assumed that there are no fluid-solid interactions. So the surface (perimeter in two dimensions) of each grain is covered with the edges of the adjacent triangular mesh elements where no-slip and no-flux boundary conditions at these edges are considered for flow and mass transport equations, respectively. The boundary conditions in the y direction, normal to the flow, are no flux for the mass

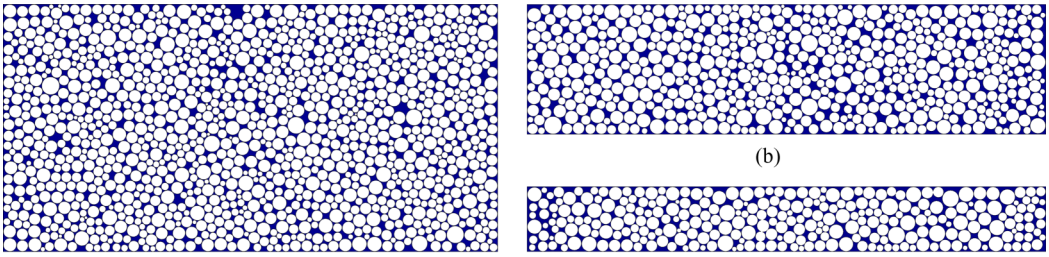

FIG. 4. Patterns with $\bar{d} = 0.3$ mm, CV $= 0.25$, $L_{\mathrm{D}} = 50$, and different A. (a) PM3 with $A = 2$, (b) PM10 with $A = 4$, and (c) PM11 with $A = 8$. Note that the patterns are depicted in the correct scales.

transfer and no-penetration/slip for fluid flow equation. The no-penetration/slip boundary condition is employed here to make sure there is no influence of boundaries on mixing. To test the convergence of numerical results regarding the spatial resolution, five different spatial resolutions of extracoarse, coarse, normal, fine, and extrafine meshes with 117 330, 260 638, 325 070, 491 340, and 1 331 485 elements, respectively, are used in a mesh-resolution sensitivity analysis in the simulation of miscible displacement in PM3 at $R = 2$ and Pe $= 400$. The results of this test show that the mesh must consist of at least 300 000 elements for the solutions to converge to the solution of the finest grid. Therefore, in all the numerical simulations of this work, we generate mesh grids with at least 450 000 elements in order to achieve both convergency and speed in the simulation runs.

III. DYNAMICS OF MIXING LENGTH GROWTH

In the dimensionless form, mixing zone length ($L_{M,\mathrm{D}}$) along the general direction of flow (here the x direction) is defined as the distance between two transversely averaged concentration values of $\bar{c}_{\mathrm{D}} = \alpha$ and $\bar{c}_{\mathrm{D}} = 1 - \alpha$ as

$$L_{M,\mathrm{D}} = |x_{\mathrm{D}}|_{\text{at } \bar{c}_{\mathrm{D}}=\alpha} - x_{\mathrm{D}}|_{\text{at } \bar{c}_{\mathrm{D}}=1-\alpha}|, \; 0 < \alpha < 1. \tag{13}$$

The transversely averaged concentration at each x_{D} can be calculated as

$$\bar{c}_{\mathrm{D}}(x_{\mathrm{D}}, t_{\mathrm{D}}) = \frac{\int c_{\mathrm{D}}(x_{\mathrm{D}}, y_{\mathrm{D}}, t_{\mathrm{D}}) dy_{\mathrm{D}}}{\int dy_{\mathrm{D}}}. \tag{14}$$

Taylor [22] and Aris [21] have shown that for dispersion-dominated miscible flow in capillary tubes, mixing length can be related to dispersion coefficient (K) along the direction of flow

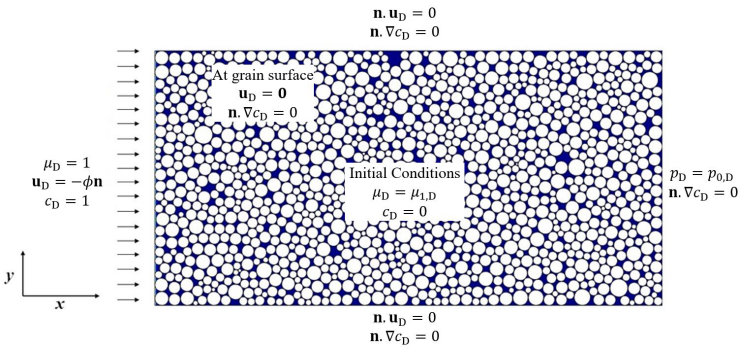

FIG. 5. Initial and boundary conditions for flow and mass transport.

(longitudinal dispersion coefficient) as

$$L_M = \beta(Kt)^{0.5}, \tag{15}$$

where β is a constant that can be obtained from any standard table of error integral for each value of α [11]. Since dispersion is the combined effect of molecular diffusion and convective spreading, the longitudinal dispersion coefficient can be described as the sum of these two mechanisms as demonstrated by Brigham *et al.* [11] and Perkins and Johnston [42] for unconsolidated sandpacks:

$$\frac{K}{D} = \frac{1}{F\phi} + a\left(\frac{v\bar{d}}{D}\right)^b. \tag{16}$$

In this equation, a is the mixing coefficient which describes the inhomogeneity of the medium at dynamic conditions, b is an exponent between 1 and 2 that depends on the type of porous medium, and F is the formation factor [11]. Substituting K from Eq. (16), Eq. (15) can be rewritten in the dimensionless form as

$$L_{M,\mathrm{D}} = \beta\left(\frac{1}{F\phi}\mathrm{Pe}^{-1} + a\mathrm{Pe}^{b-1}\right)^{0.5} {t_\mathrm{D}}^{0.5}. \tag{17}$$

If t'_D is defined as $t'_\mathrm{D} = t_\mathrm{D}/L_\mathrm{D}$, which represents the value of pore volume injected (PVI) into porous media, Eq. (17) can be rewritten as

$$L_{M,\mathrm{D}} = \beta {L_\mathrm{D}}^{0.5}\left(\frac{1}{F\phi}\mathrm{Pe}^{-1} + a\mathrm{Pe}^{b-1}\right)^{0.5} {t'_\mathrm{D}}^{0.5}. \tag{18}$$

Equation (18) suggests that mixing length will grow proportional to square root of time ($L_{M,\mathrm{D}} \sim {t'_\mathrm{D}}^{0.5}$). This is Fickian dispersion, and its associated flow is called dispersive flow, which occurs when mixing is complete in the transverse direction. However, as soon as viscous fingering arises, mixing is not Fickian anymore and mixing length scales with time as

$$L_{M,\mathrm{D}} \sim {t'_\mathrm{D}}^{\sigma}. \tag{19}$$

In Eq. (19), σ is the growth exponent of mixing length, which depends on the transport mechanism, flow instabilities, and medium heterogeneity. We employ Eq. (19) to extract the values of the growth exponent (σ) as the main indicator of the flow and transport behavior during miscible displacements. First, we obtain the concentration maps at different times by solving the flow and mass transport equations on the images of the constructed porous media. Then the values of mixing length are calculated as Eq. (13) (with $\alpha = 0.05$) and plotted against time. Finally, σ is obtained by fitting a power-law trend line on the $L_{M,\mathrm{D}}$ versus t'_D plots.

A. Validation of the numerical approach

To validate the presented pore-scale numerical approach, we simulate the stable ($R = 0$) miscible displacement in a capillary tube and between two parallel plates. From the analytical solutions of the one-dimensional convection-dispersion equation during flow in a capillary tube [21,22] and flow between two parallel plates [43], one can easily show that mixing length scales with the square root of time during stable miscible displacements. Figure 6 shows how the growth of mixing length, obtained by our numerical simulations, compares to the analytical solutions (with $\alpha = 0.05$) at two different values of the Péclet number. In the analytical solutions shown in Fig. 6, Pe^* is the macroscale Péclet number defined as $\mathrm{Pe}^* = u_m l_c/K_L$, Pe is the pore-Péclet number defined as $\mathrm{Pe} = u_m l_c/D$, u_m is the mean velocity, l_c is the characteristic length (half-aperture for the parallel plates geometry and radius for the capillary tube), and K_L is the longitudinal dispersion coefficient. As the comparison demonstrates, the numerically obtained mixing length ($L_{M,\mathrm{D}}$) and its growth exponent (σ) are in a very close agreement with the analytical solutions in both geometries.

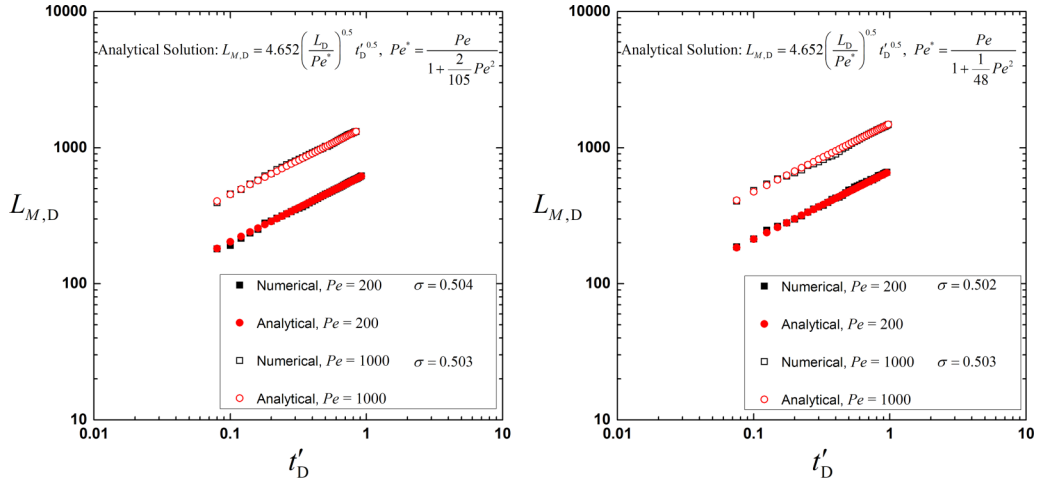

FIG. 6. Temporal variation of mixing length during miscible displacement (a) between two parallel plates and (b) in a capillary tube with $L_D = 5000$. The growth exponent (σ) compares perfectly with the expected value of 0.5 [10,11,21,22].

B. Effect of viscosity ratio on mixing length growth

A series of simulations are run in medium PM3 at different R and Pe values to investigate the effect of viscosity ratio on the growth of mixing length. We identify the intensity of fingering through tracking of concentration iso-surfaces, herein referred to as concentration front or solution interface. Then the temporal variation of mixing length is used to characterize the type of transport regime.

Figures 7 to 9 illustrate the spatiotemporal profiles of concentration during unstable displacements at R values of 0 to 4 and three different Péclet numbers equal to 0.2, 20, and 2000. Each figure consists of displacement results for t'_D values of 0.1, 0.3, and 0.5. At very low Pe (Fig. 7), the solution interface remains close to diffusive as small disturbances induced by viscosity contrast do not turn into advancing fingers within the domain even at high values of R. Thus, a slightly distorted interface is observed in the case of Pe $= 0.2$. As Pe increases (Figs. 8 and 9), the effects of adverse viscosity ratio and medium heterogeneity come into play, and both heterogeneity-induced channeling and viscous fingering occur and give rise to the non-Fickian transport regime. When the viscosity ratio is unity [Figs. 8(a) and 9(a)], small-scale channelings due to the microscale heterogeneity of medium occur and result in preferred paths for solute transport at the leading edge of the concentration front. These preferred paths are the ones with the least resistance to flow and transport inside the porous medium. At adverse viscosity ratios [Figs. 8(b)–8(e) and Figs. 9(b)–9(e)], viscous fingering is the dominant transport regime and the development of the fingers results in larger mixing zones. As R increases, the longitudinal extent of the fingers also increases, thus higher values for $L_{M,D}$ are expected.

Next, we use the transversely averaged concentration profiles, evaluated per Eq. (14), to calculate $L_{M,D}$. Figure 10 shows the $L_{M,D}$ values plotted against time on a logarithmic scale for Pe values of 0.2, 2, 200, 400, 1350, and 2000. The plots indicate that for all cases, $L_{M,D}$ linearly increases with t'_D in a log-log plot, hence Eq. (19) represents the scaling of mixing length with time. To better visualize the magnitude of σ, two guide lines representing the slopes of 0.5 and 1.0 are also embedded on each plot (as dash and solid lines, respectively). Figures 10(a)–10(f) disclose that the slope of mixing length plots, i.e., σ, is always between the two extremes of 0.5 (corresponding to dispersive flow) and 1.0 (representing the fingering regime). A power-law trend line is fitted on each plot, and the numerical values of the growth exponent (σ) are reported in Fig. 11. For the case of Pe $= 0.2$ [Fig. 10(a)], $L_{M,D}$ values for all mobility ratios collapse to a single plot with σ in the

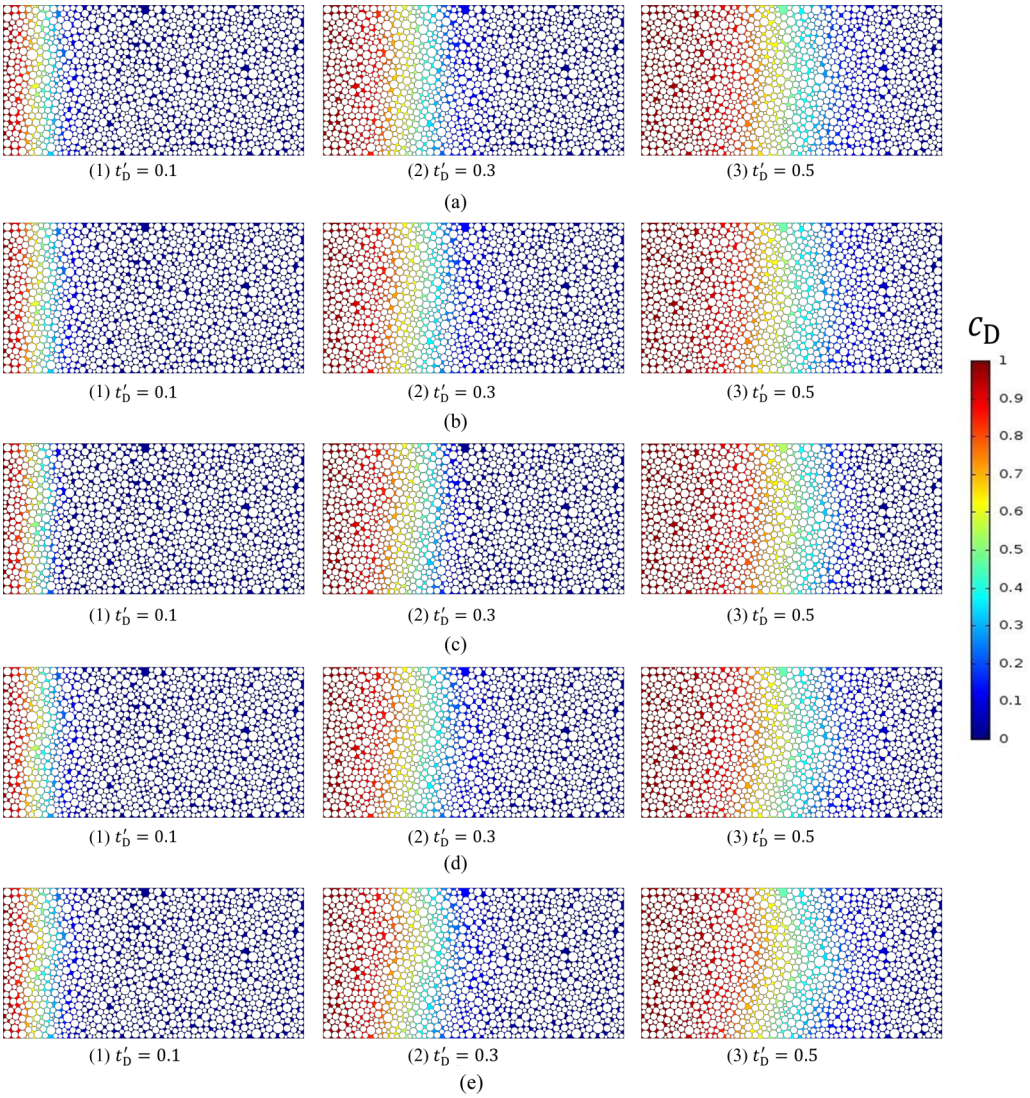

FIG. 7. Spatiotemporal profiles of c_D at Pe $= 0.2$ for medium PM3. (a) $R = 0$, (b) $R = 1$, (c) $R = 2$, (d) $R = 3$, and (e) $R = 4$.

range of 0.55–0.6 (Fig. 11) confirming the observed close to dispersive transport regime in Fig. 7. The magnitude of Péclet number is so low that there is enough time for dispersion to homogenize the concentration profile in the transverse direction and attenuate the viscous instabilities. This is consistent with the previous linear stability analysis [35,36] and numerical simulations [12], which show that for each R, there is a critical Péclet number below which displacement is dispersive despite the adverse viscosity ratio. As Pe increases to values larger than 2, the effect of viscosity ratio becomes significant and $L_{M,D}$ increases with R [Figs. 10(b)–10(f)]. This is also followed by larger values for σ, which increases with R with a steep slope (almost linear) until $R = 3$ and with a less steep slope for $R > 3$ as shown in Fig. 11. One may conclude that the values of critical Péclet numbers for the simulations of this study are between 0.2 and 2. Another observation is that for sufficiently large Péclet numbers (Pe $\geqslant 400$), mixing length and its growth exponent are independent of Pe. This behavior is also confirmed by previous studies in Darcy scale [18,19] and indicates that the nonlinear

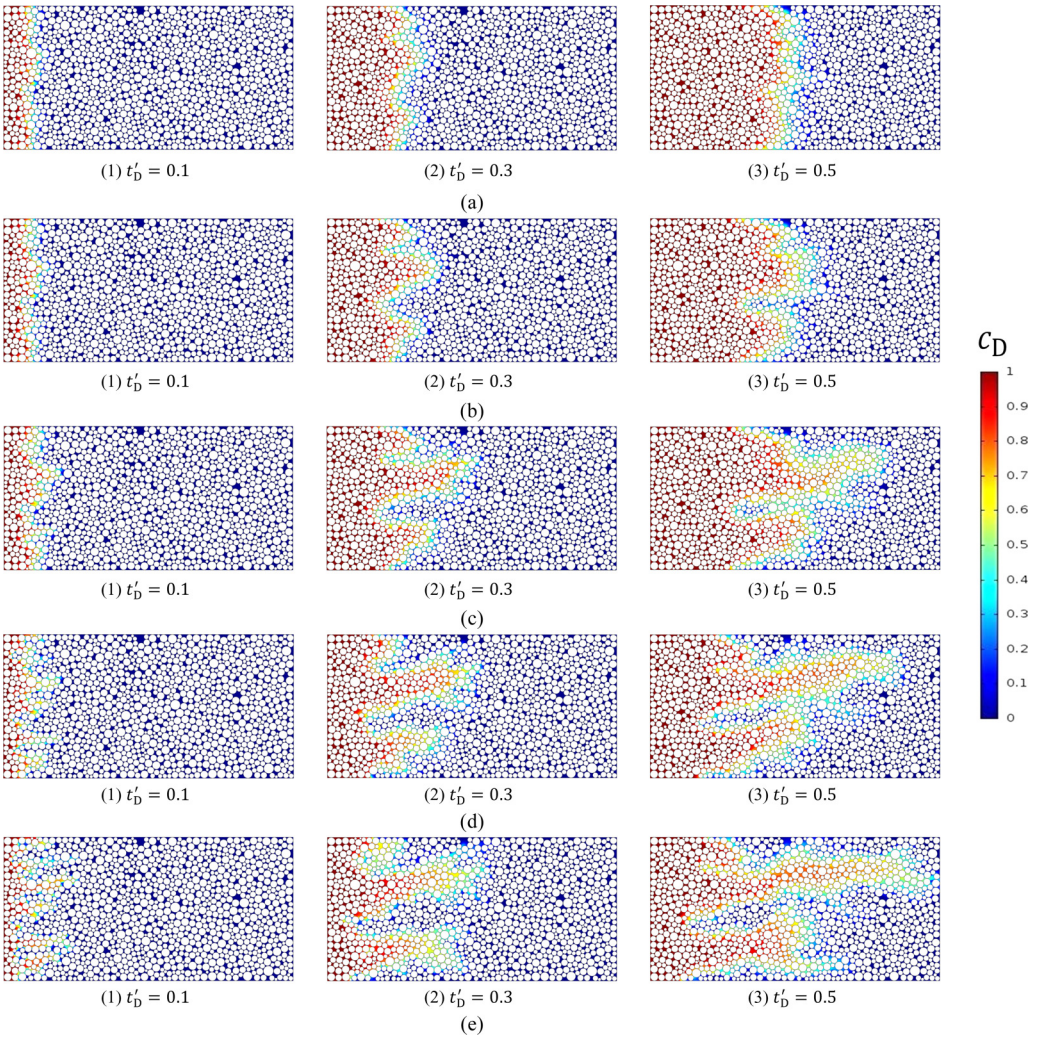

FIG. 8. Spatiotemporal profiles of c_D at Pe = 20 for medium PM3. (a) $R = 0$, (b) $R = 1$, (c) $R = 2$, (d) $R = 3$, and (e) $R = 4$.

dynamics of viscous fingering are governed by pressure field resulting from the viscosity contrast and is independent of the dispersion magnitude.

As reported in the literature [12,13,19,25,28–30], mixing length varies linearly in time and the growth exponent is 1.0 for the unstable displacement in a homogeneous medium. In the presence of heterogeneity, the growth exponent is reported to be either 0.5 or 1.0 depending on the variance and correlation length of the permeability field [12,18,23,34]. The results of our simulations at pore scale, however, indicates that σ has a value between 0.5 and 1.0 for an inherently heterogeneous medium depending on the magnitudes of R and Pe (Fig. 11). The difference between the results of macroscale and pore-scale simulations may originate from the fact that in macroscale (i.e., Darcy-scale) simulations, Eq. (3) was used with a dispersion coefficient rather than molecular diffusion coefficient. This dispersion coefficient usually has been considered to be either a constant or dependent on the velocity with a linear [28,44] or quadratic [29,44] relationships. However, the experiments of Brigham *et al.* [11] show that the dispersion coefficient depends on velocity as $K \sim v^b$, where $1 < b < 2$. In our pore-scale simulations, we use point equations (Navier-Stokes

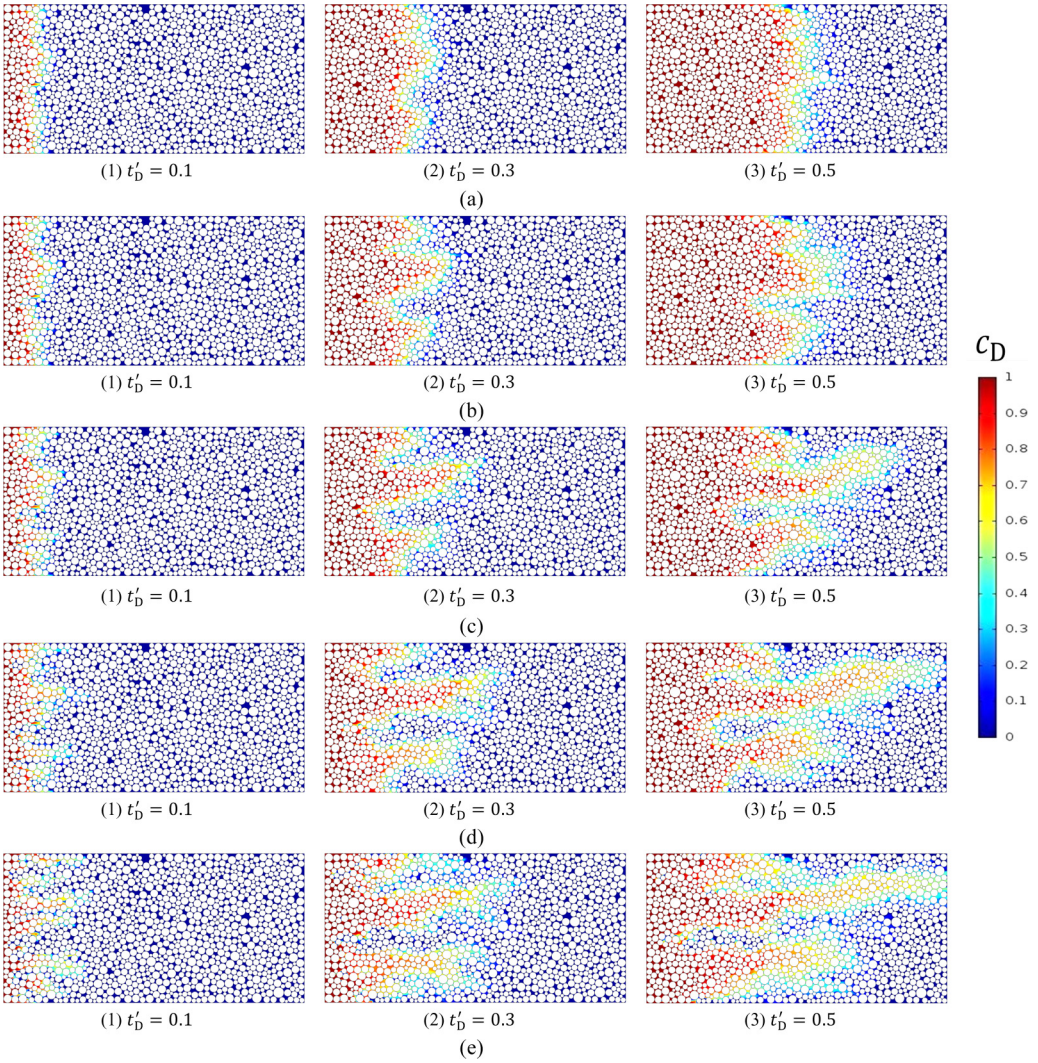

FIG. 9. Spatiotemporal profiles of c_D at Pe = 2000 for medium PM3. (a) $R = 0$, (b) $R = 1$, (c) $R = 2$, (d) $R = 3$, and (e) $R = 4$.

and convection-diffusion) rather than Darcy-scale equations (Darcy flow and convection-dispersion). Thus, the level of dispersion considered in pore-scale simulations is closer to reality compared to that of macroscale simulations.

C. Effect of heterogeneity on mixing length growth

We next examine the effect of medium heterogeneity on σ for both stable and unstable displacements with the primary emphasis on the heterogeneity of grain size distribution represented by CV. Miscible displacement simulations are performed on the media PM1 to PM4, with a CV of 0, 0.125, 0.25, and 0.5, respectively, at different Pe and two values of $R = 0$ and $R = 3$. For the sake of brevity, we skip the qualitative presentation of concentration iso-surfaces and report only the quantitative results. In the case of stable displacement ($R = 0$), the objective is to study the sole effect of medium heterogeneity on mixing length growth in the absence of any fingering, while the interaction of heterogeneity and fingering is explored during the unstable displacements at $R = 3$.

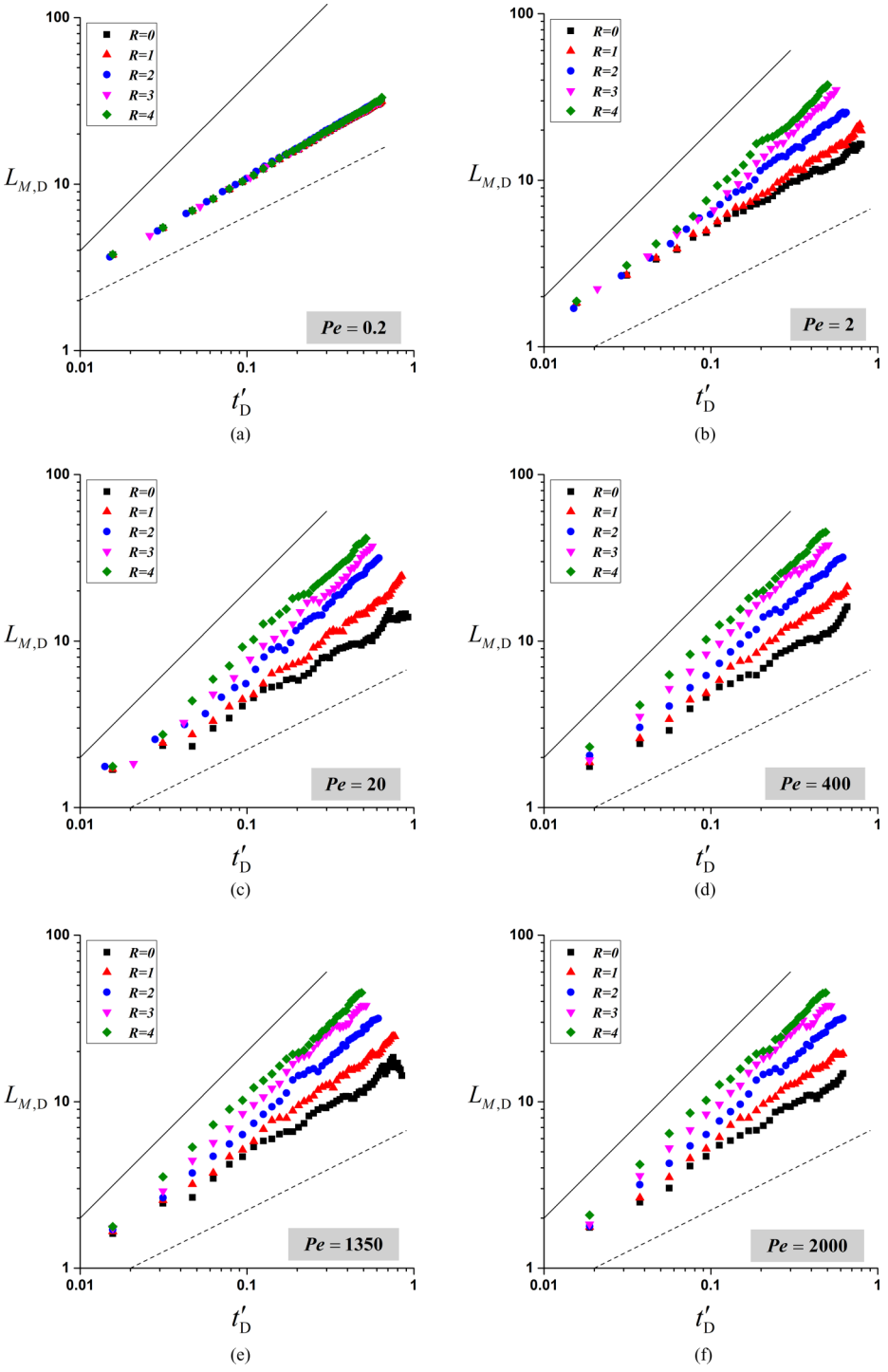

FIG. 10. Log-log plots of the mixing length temporal variations during miscible displacement in medium PM3 at different viscosity ratios and (a) Pe = 0.2, (b) Pe = 2, (c) Pe = 20, (d) Pe = 400, (e) Pe = 1350, and (f) Pe = 2000. The guide lines with slopes 0.5 and 1.0 are also plotted as straight dash and solid lines, respectively.

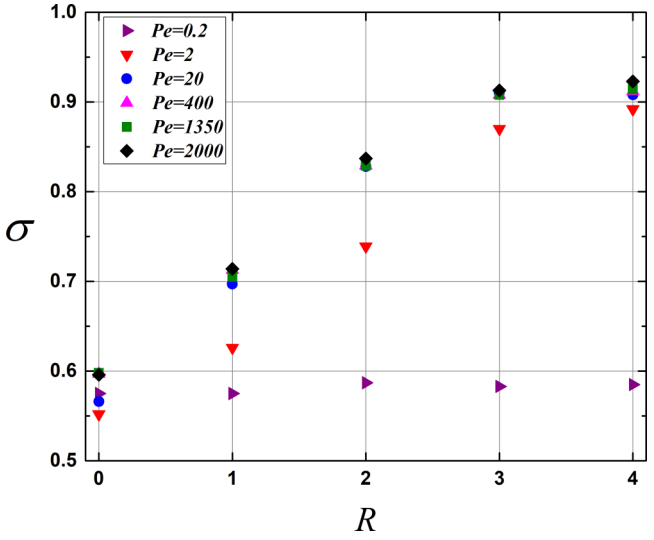

FIG. 11. Mixing length growth exponent versus log-viscosity ratio for medium PM3 (CV = 0.25) at different Péclet numbers.

Figures 12 and 13, respectively, depict the temporal variations of mixing length at $R = 0$ and 3 on a log-log scale for Pe values of 0.2, 2, 20, 400, and 2000. For different values of Pe and R, the mixing length generally increases with CV demonstrating the fact that a higher level of heterogeneity results in a larger mixing zone. The values of the growth exponent corresponding to the plots of Figs. 12 and 13 are also reported in Figs. 14 and 15, respectively. For the case of unit viscosity ratio (Fig. 14), the growth exponent varies nonmonotonically with both Pe and the level of heterogeneity as σ is the largest at CV values of 0 and 0.25 while for all CV, σ is minimum at Pe = 2. For the unstable displacement case (Fig. 15), $\sigma -$ CV variation is also nonmonotonic, with the higher values for CV = 0 and 0.25. Unlike $R = 0$, the growth exponent monotonically increases with the Péclet number, and the minimum in $\sigma -$ Pe plot vanishes in the unstable displacement cases at $R = 3$.

The nonmonotonic behavior of $\sigma -$ CV is counterintuitive and raises the point that whether CV is sufficient for representing the medium heterogeneity. In macroscale permeability distributions, it is a common practice to characterize the permeability heterogeneity with a variance representing the degree of variations and a correlation length describing the spatial correlation. In our pore-scale media, CV as defined in Eq. (12) can be the measure of heterogeneity, but it is difficult to describe the correlation of heterogeneity based on the grain size distribution. Therefore, we employed another approach to characterize the heterogeneity of our models based on the distribution of velocity. The heterogeneity of a porous medium results in a nonuniform velocity distribution, and consequently the variation of this velocity distribution can be an approximate measure of the heterogeneity. Accordingly, we extract the velocity distribution for each medium and describe its heterogeneity by the standard deviation ($S_{|u_{x,\mathrm{D}}|}$) of the distribution and the correlation length (λ_D) of the velocity variogram. The calculated $S_{|u_{x,\mathrm{D}}|}$ and λ_D for each medium are reported in Table II along with their

TABLE II. The parameters describing the heterogeneity of patterns.

Pattern name	CV	$S_{\lvert u_{x,\mathrm{D}}\rvert}$	λ_D
PM1	0	1.27	∼3.4
PM2	0.125	1.32	∼2.7
PM3	0.25	1.38	∼2.6
PM4	0.5	1.32	∼2.1

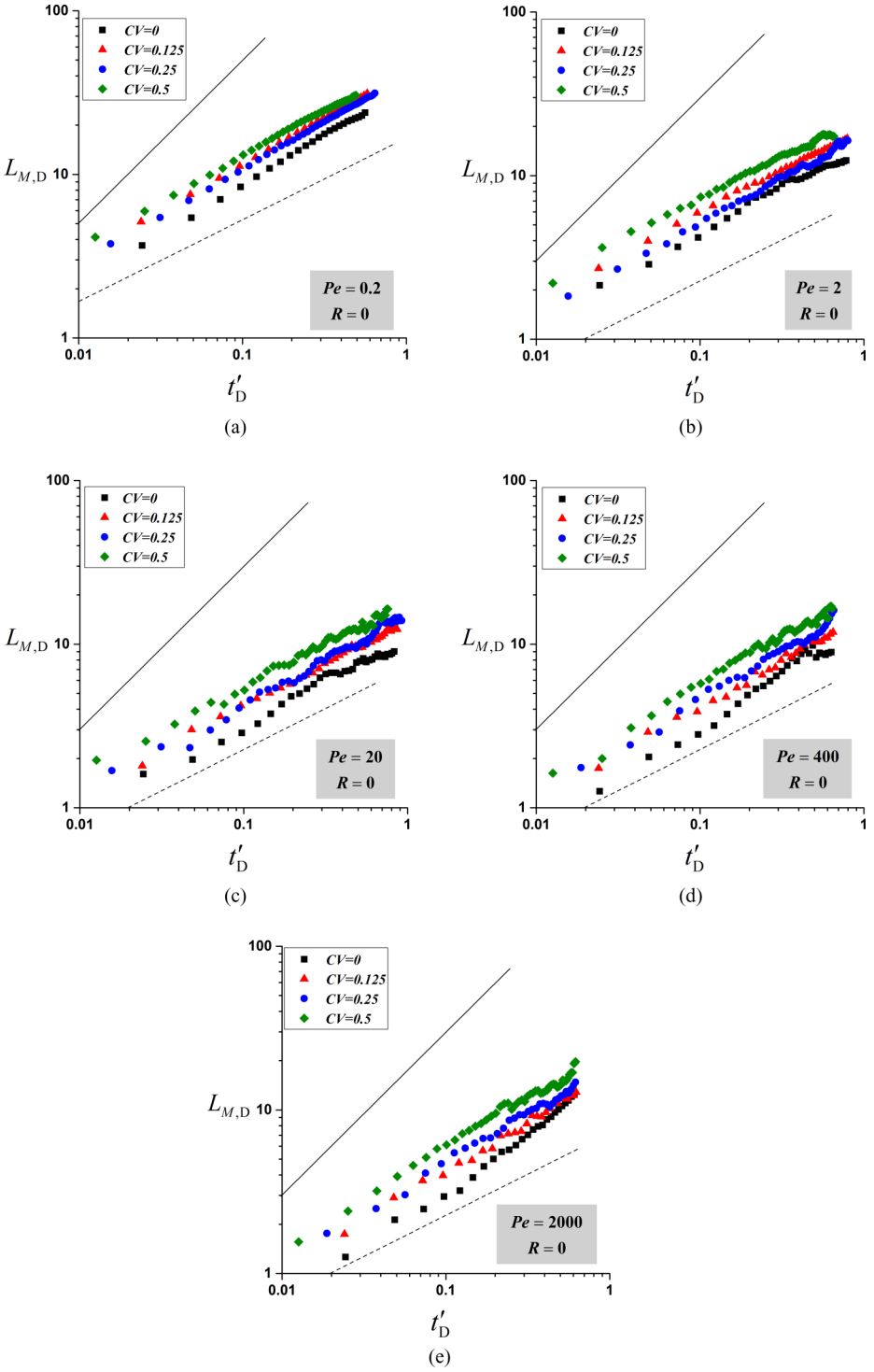

FIG. 12. Log-log plots of the mixing length temporal variations during miscible displacement in media PM1 to PM4 at $R = 0$ and (a) Pe $= 0.2$, (b) Pe $= 2$, (c) Pe $= 20$, (d) Pe $= 400$, and (e) Pe $= 2000$. The guide lines with slopes 0.5 and 1.0 are also plotted as straight dash and solid lines, respectively.

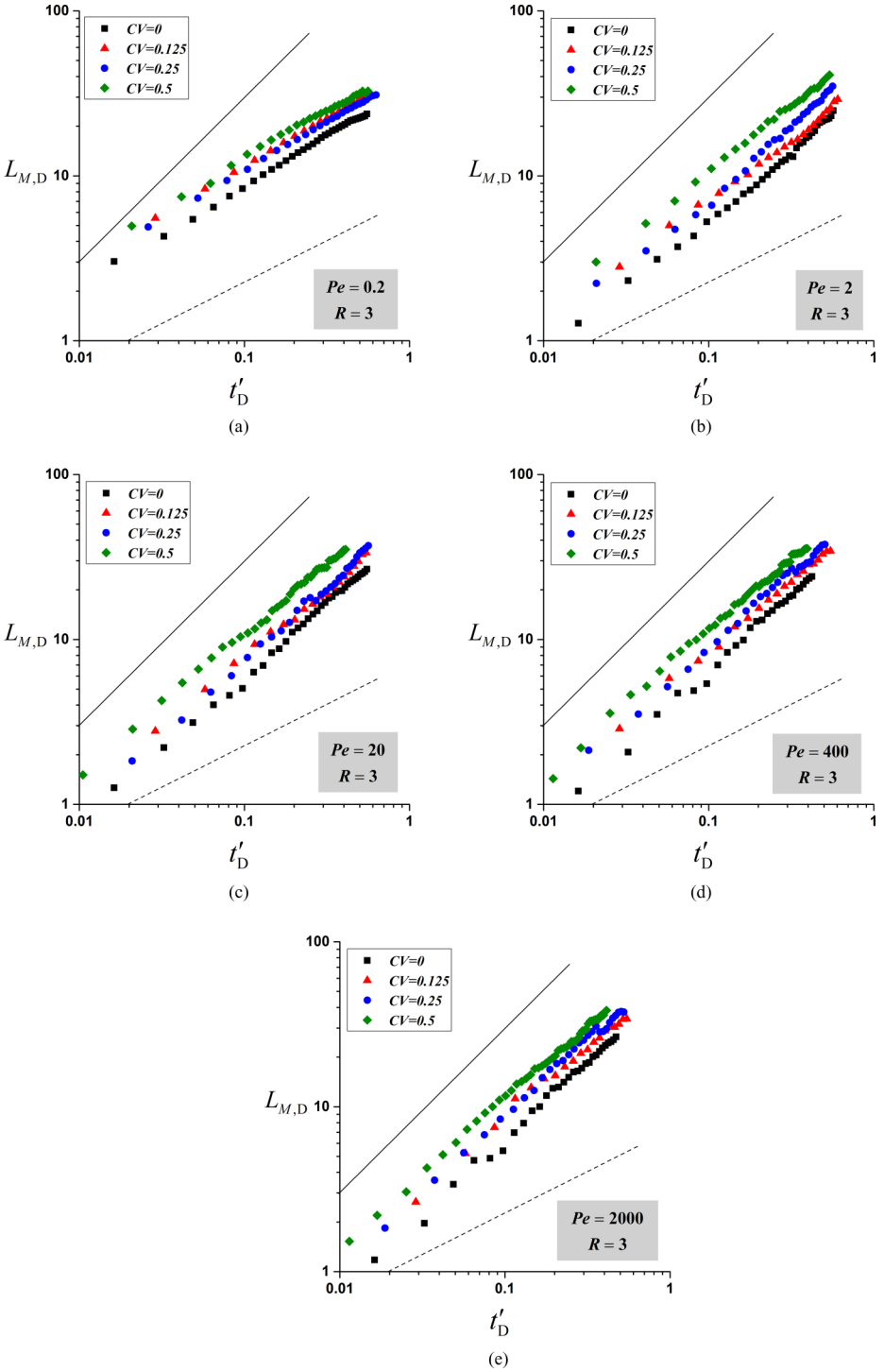

FIG. 13. Log-log plots of the mixing length temporal variations during miscible displacement in media PM1 to PM4 at $R = 3$ and (a) Pe = 0.2, (b) Pe = 2, (c) Pe = 20, (d) Pe = 400, and (e) Pe = 2000. The guide lines with slopes 0.5 and 1.0 are also plotted as straight dash and solid lines, respectively.

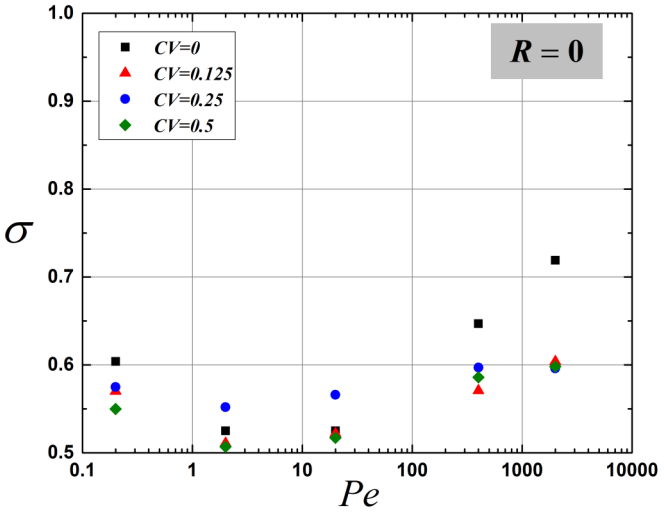

FIG. 14. Mixing length growth exponent versus Péclet number for media PM1 to PM4 at $R = 0$.

CV. Details of the calculation of these parameters can be found in the Appendix. The analysis of the correlation structure of velocity and porosity reveals that the correlation length is much smaller than the medium length, hence suggesting that our patterns are large enough to be representative of real sandpacks. Moreover, λ_D decreases with CV, and its value is the highest for medium PM1. This is because for a smaller CV, the distribution of grain size is narrower, and when the pattern is being generated, there are fewer options for grain sizes. This makes it difficult to place the grains at completely random locations within a pattern and may introduce some preferred channels for the flow. As an illustration, Fig. 16 shows the spatial concentration profiles for the media PM1 to PM4 during miscible displacement at $R = 3$. At smaller CV [Figs. 16(a) and 16(b)], viscous fingers are following some prominent paths that are the result of higher correlation lengths, while for higher CV [Figs. 16(c) and 16(d)], there are no clear paths for viscous fingers as they are developed across

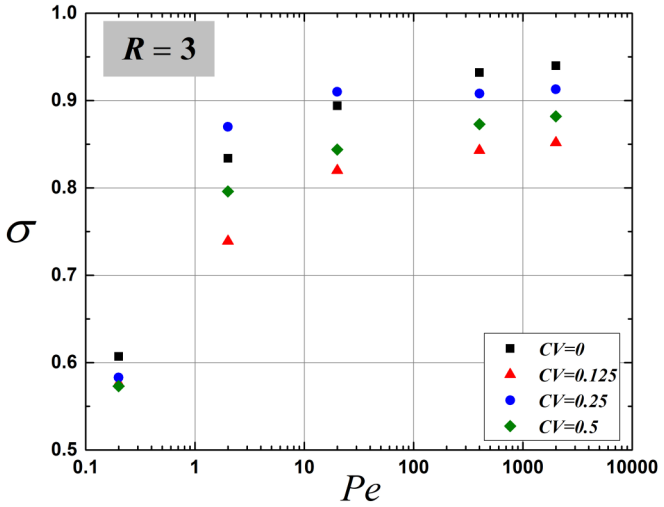

FIG. 15. Mixing length growth exponent versus Péclet number for media PM1 to PM4 at $R = 3$.

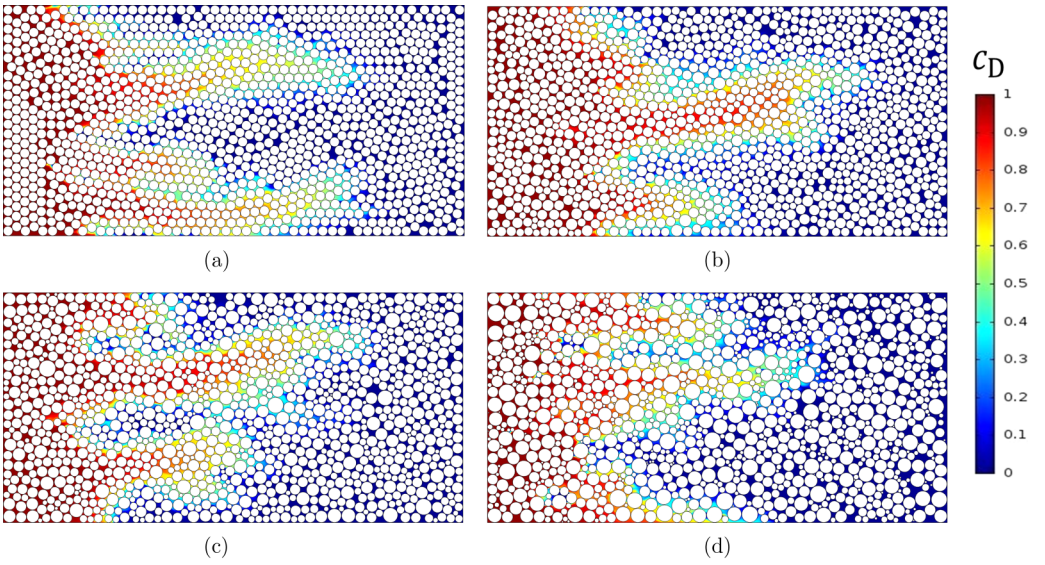

FIG. 16. Spatial profiles of c_D at $t'_D = 0.4$ during miscible displacement at $R = 3$ and Pe $= 400$ in (a) PM1, (b) PM2, (c) PM3, and (d) PM4.

the entire width of the patterns. Based on these new measures of heterogeneity, PM1 and PM3 have the highest heterogeneity in terms of correlation length and velocity distribution, respectively.

Table II shows that PM1 has a considerably larger λ_D compared to the other patterns, while PM3 has a higher $S_{|u_{x,D}|}$ with a λ_D approximately similar to that of PM2 and larger than that of PM4. According to Figs. 14 and 15, the growth exponent is generally higher for media PM1 and PM3 even though their CV are smaller than the CV of PM4. Such an observation is consistent with the $S_{|u_{x,D}|}$ and λ_D trends in these media. Thus, we conclude that although the size of the mixing zone generally increases with CV, its growth is primarily governed by velocity variation and correlation length rather than CV.

IV. SCALING AND GENERALIZATION OF MIXING LENGTH PLOTS

The similarities between $L_{M,D}$ temporal variations for different values of R and CV in Figs. 10, 12, and 13 give the idea that it is possible to obtain a general curve describing the variation of mixing length with time for any arbitrary values of R and CV. To accomplish this, we try to scale the mixing length plots with R and CV as well as the geometrical parameters of medium length (L_D) and medium aspect ratio (A). The compact form, when achieved, is useful in engineering calculations; however, we should note that the scaling may not necessarily work for all regions of parameter space.

A. Scaling of viscosity ratio (R)

As presented in Fig. 10, $L_{M,D}$ increases with log-viscosity ratio when Pe $\geqslant 2$. For layered permeability fields, Sajjadi and Azaiez [17] proposed that mixing length can be scaled by $e^{R/3.1}$ to account for different values of R. Using a similar functionality, we found that $L_{M,D}$ scales with $e^{R/3.5}$ for the case of random packing of grains considered in this study. Figure 17 shows the linear plots of $L_{M,D}$ growth in time, unscaled on the left and scaled on the right, for the simulations of miscible displacement in PM3 at three Péclet numbers of 2, 400, and 2000. According to the results, this scaling enables us to approximately superimpose the plots of mixing length on each other, especially at early times of displacement at high Péclet numbers [Figs. 17(b2) and 17(c2) compared to Fig. 17(a2)]. At high values of Pe, the growth of mixing length is primarily governed

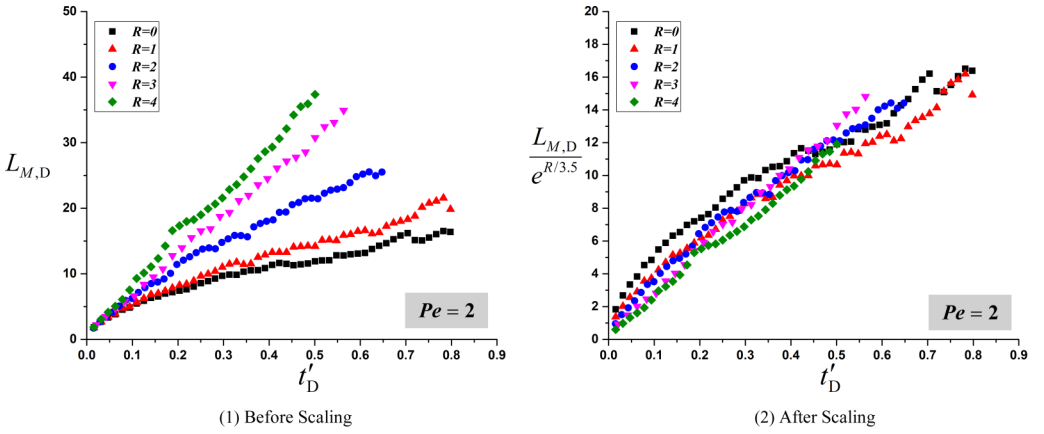

(1) Before Scaling (2) After Scaling

(a)

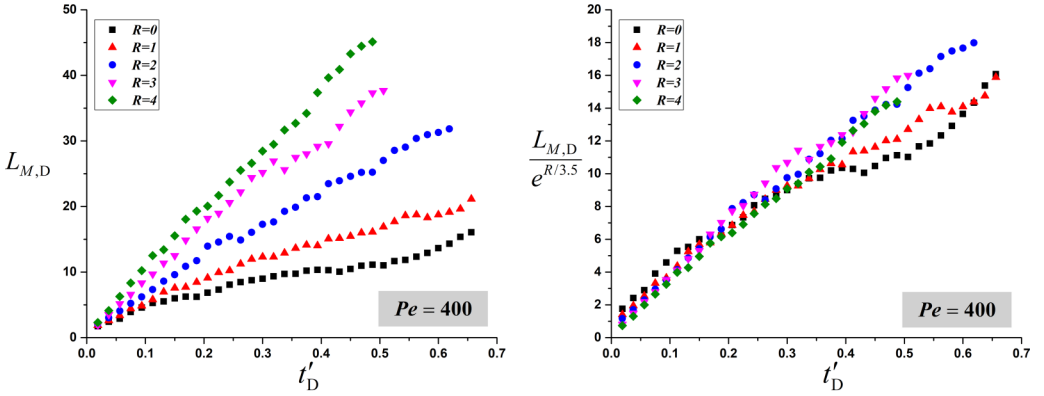

(1) Before Scaling (2) After Scaling

(b)

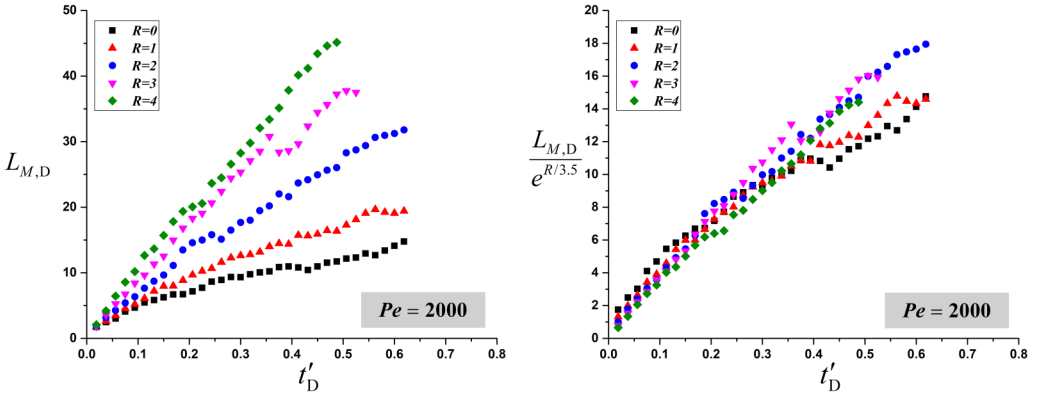

(1) Before Scaling (2) After Scaling

(c)

FIG. 17. Scaling of R for the mixing length plots of miscible displacements in PM3 at (a) Pe = 2, (b) Pe = 400, and (c) Pe = 2000. The left-side plots show the variations of mixing length before scaling while the right-side plots correspond to variations after scaling.

by viscous fingering and the effect of other parameters like local variations of heterogeneity, and the level of dispersion on mixing length is minimal compared to their impact at lower Péclet numbers. Therefore, the scaling of viscosity ratio alone is sufficient for high Pe while it may be suboptimal for low Pe values. Also, as illustrated in Figs. 17(b2) and 17(c2), at later times of displacement, the values of mixing length for $R = 0$ and 1 slightly deviate from the general trend of other plots. We propose the same rationale that at these low adverse viscosity ratios, the effect of other parameters like heterogeneity and dispersion is comparable to viscous fingering, thus making the sole scaling of R to be suboptimal.

B. Scaling of heterogeneity (CV)

Figures 12 and 13 showed that $L_{M,\mathrm{D}}$ generally increases with CV at different values of Pe during both stable and unstable displacements, respectively. These plots of mixing length for different values of CV can be collapsed on each other by scaling the values of $L_{M,\mathrm{D}}$ to e^{CV}. In Fig. 18 the results of this scaling are presented by comparing the mixing length plots before and after the scaling (left and right plots, respectively) for both stable [Figs. 18(a) and 18(b)] and unstable [Figs. 18(c) and 18(d)] flows at $\mathrm{Pe} = 0.2$ and $\mathrm{Pe} = 2000$. It can be concluded that the scaling to e^{CV} results in an approximately unified mixing length curve, especially when the effect of dispersion on mixing length is minimal at a high Péclet number or an adverse viscosity ratio.

C. Scaling of medium length (L_{D}) and aspect ratio (A)

For a dispersive transport regime (i.e., $\sigma = 0.5$), Eq. (18) implies that the plots of $L_{M,\mathrm{D}}$ versus t'_{D} should scale with the square root of medium length (L_{D}). For a fingering transport regime, however, there is no theory that describes the variation of mixing length with the porous medium length. In order to explore how mixing length plots vary with L_{D}, several patterns with different values of L_{D} are generated and used in the simulations (Fig. 3). The patterns PM3, PM5, PM6, and PM7 have the same $\bar{d}$, CV, and A, but different L_{D}, while PM8 and PM9 have different $\bar{d}$ compared to the others (see Table I). The left-hand side plots of Fig. 19 show the results of simulations in terms of mixing length plots for both stable and unstable displacement. For the stable flow ($R = 0$), simulations are performed at $\mathrm{Pe} = 0.2$ [Fig. 19(a)] and $\mathrm{Pe} = 2000$ [Fig. 19(b)], while unstable displacements are simulated at $R = 4$ and $\mathrm{Pe} = 2000$ [Fig. 19(c)]. Figures 19(a) and 19(b) demonstrate that the plots of mixing length approximately scale with ${L_{\mathrm{D}}}^{0.5}$ for the stable displacements as predicted by Eq. (18). For miscible displacements at adverse viscosity ratio, however, mixing length scales almost linearly with medium length [Fig. 19(c)], and dividing $L_{M,\mathrm{D}}$ by L_{D} results in an approximate unified curve that can be employed to predict the mixing length value for any arbitrary L_{D}.

To examine the effect of aspect ratio (A) on mixing length, both unit and adverse viscosity ratio displacements are simulated in media PM3, PM10, and PM11 which have aspect ratios of 2, 4, and 8, respectively (Fig. 4). The other properties of these media are similar to each other as summarized in Table I. The results of simulations (Fig. 20) reveal that the aspect ratio has an insignificant impact on mixing length in both stable and unstable displacements, and therefore it is not necessary to consider the aspect ratio in our scaling and unification of the mixing length plots.

V. SUMMARY AND CONCLUSION

Direct pore-scale simulations of miscible displacement in two-dimensional heterogeneous unconsolidated porous media are conducted to investigate the effect of flow velocity, viscosity ratio, and pore-scale heterogeneity of media on the growth of the mixing zone. The microscale heterogeneity is characterized by three parameters: a coefficient of variation defined as the standard deviation of the grain size (CV), standard deviation of the velocity field ($S_{|u_{x,\mathrm{D}}|}$), and its correlation length (λ_{D}). The effect of flow velocity is incorporated in a pore-Péclet number (Pe) while viscosity contrast is described by the log-viscosity ratio (R). Several pore-scale patterns are generated and used in the numerical simulations to obtain the temporal variation of the mixing length ($L_{M,\mathrm{D}}$). Then

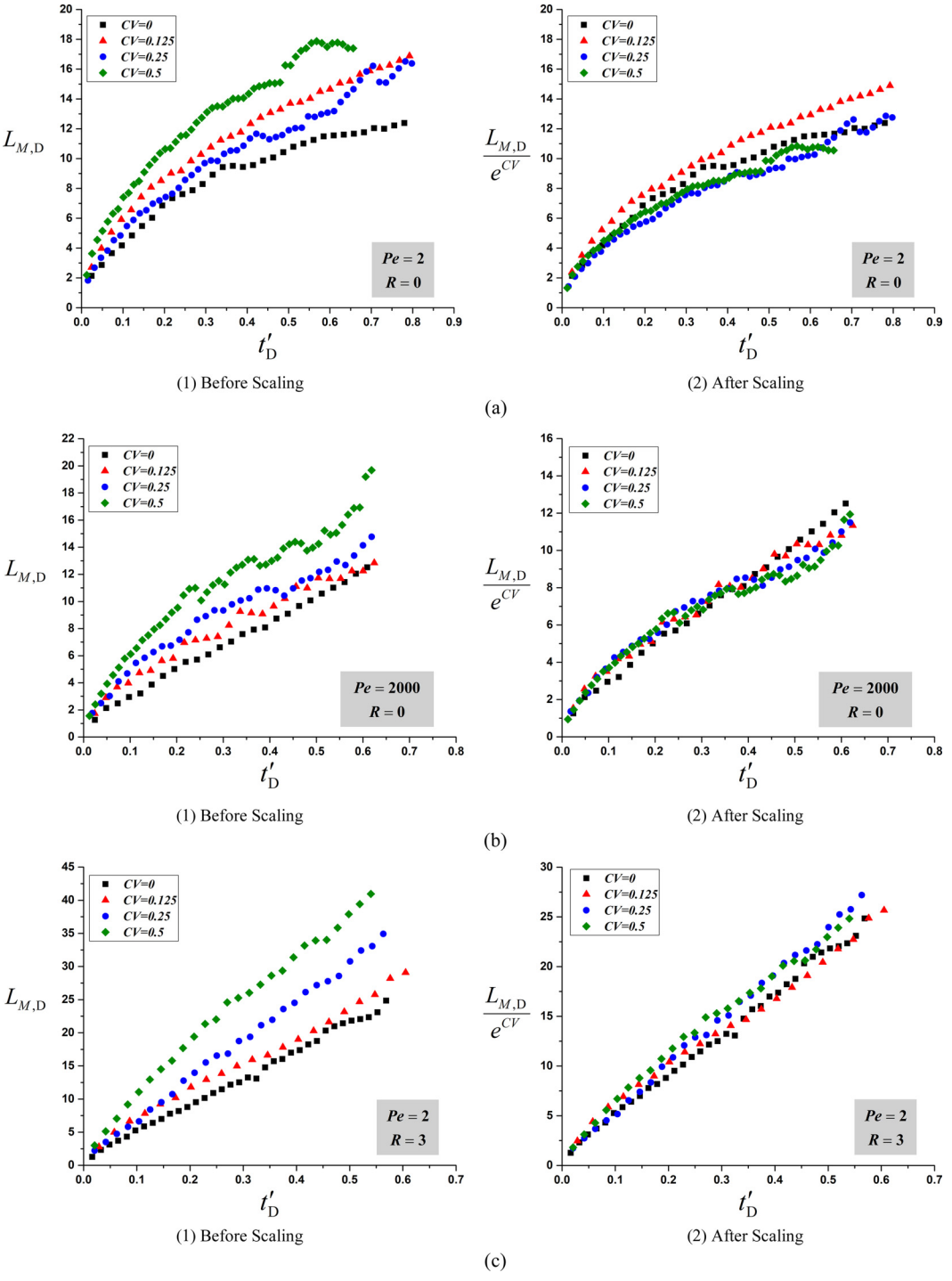

FIG. 18. Scaling of CV for the mixing length plots of miscible displacements in PM1 to PM4 at (a) $R = 0$ and Pe $= 2$, (b) $R = 0$ and Pe $= 2000$, (c) $R = 3$ and Pe $= 2$, and

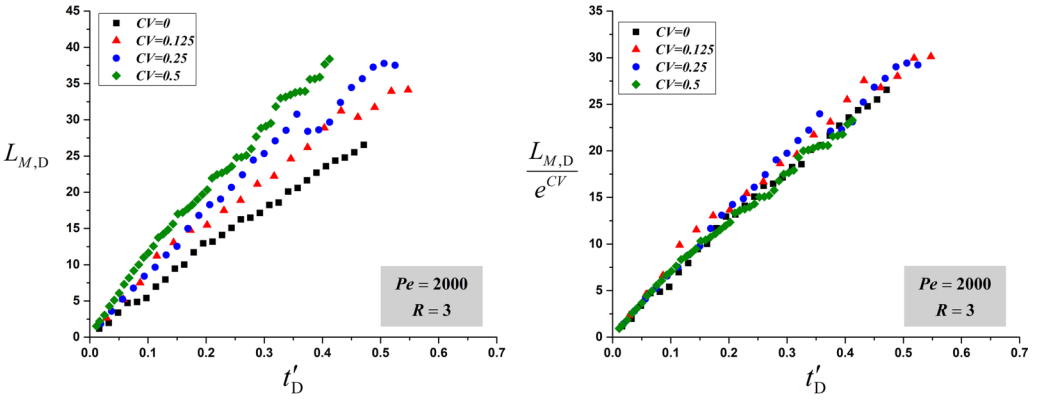

(d)

FIG. 18. (*Continued.*) (d) $R = 3$ and Pe $= 2000$. The left-side plots show the variations of mixing length before scaling while the right-side plots correspond to variations after scaling.

a power-law trend line is fitted on the mixing length plots and the values of mixing length growth exponent (σ) are extracted and plotted against the governing parameters.

Through this study, it is concluded that viscosity ratio and heterogeneity have different effects on the growth of mixing length at different Péclet numbers. Their interactions dictate whether the flow and transport mechanism is dispersive or fingering. The results indicate that for each value of R, there is a critical Péclet number below which there is no effect of viscosity contrast on mixing length growth and the transport regime remains dispersive. As Pe exceeds this critical value, the mixing length gets larger as R increases and its growth exponent linearly increases with viscosity ratio up to $R = 3$. At sufficiently large Pe, both $L_{M,\mathrm{D}}$ and σ are independent of Pe because dispersion becomes irrelevant at these large Péclet numbers and fingering is mainly governed by pressure field. Contrary to the linear growth of $L_{M,\mathrm{D}}$ in a fingering flow at macroscale permeability maps, the results of pore-scale displacements indicate that σ has always a value between 0.5 and 1.0 even for high adverse viscosity ratios. Numerical simulations in media with different levels of microscale heterogeneity demonstrate that $L_{M,\mathrm{D}}$ increases with CV at all values of Pe while the growth exponent is generally higher for the media with larger λ_{D} and $S_{|u_{x,\mathrm{D}}|}$.

To construct a generalized curve that describes the temporal variation of mixing length for all combinations of governing parameters, we attempt to scale the values of $L_{M,\mathrm{D}}$ with R, CV, medium length (L_{D}), and aspect ratio (A). The results of the scaling procedure imply that $L_{M,\mathrm{D}}$ scales approximately with e^R and e^{CV} for both stable ($R = 0$) and unstable ($R > 0$) displacements. In the unit viscosity ratio flow, mixing length approximately scale with ${L_{\mathrm{D}}}^{0.5}$ while at adverse viscosity ratio it scales with L_{D}. Finally, it is shown that mixing length is not dependent on the aspect ratio and it can be ignored in the process of scaling.

ACKNOWLEDGMENTS

We acknowledge G. M. (Bud) Homsy for reviewing the first draft and numerous fruitful and enlightening comments and discussions. We also thank Saeed Taheri for providing the grain arrangement code. The authors acknowledge the financial support of the FUR program from NSERC, AITF/i-CORE, and the sponsoring companies: Athabasca Oil Corporation, Laricina Energy Ltd., Devon Canada, Foundation CMG, Husky Energy, Brion Energy, Canadian Natural, Maersk Oil, Suncor Energy, and Schulich School of Engineering (University of Calgary). S.H.H. also acknowledges the Imperial Oil University Research Award and NSERC Discovery Grant.

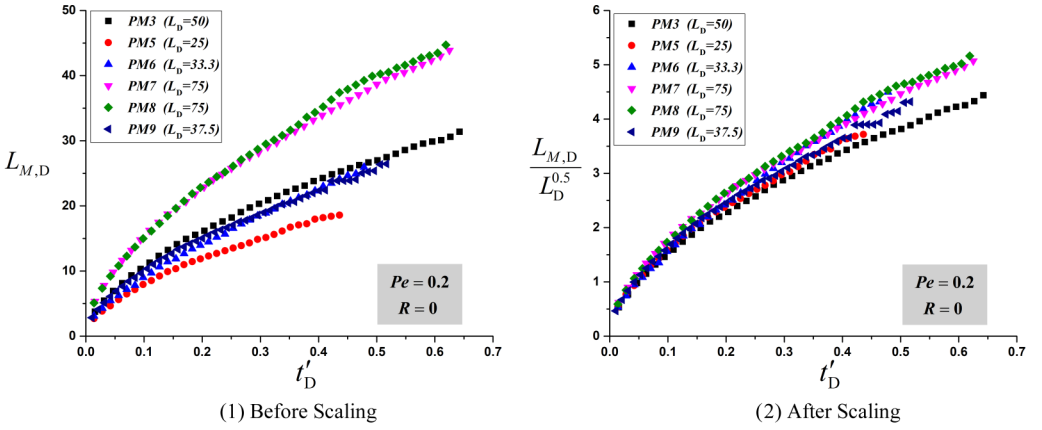

(1) Before Scaling (2) After Scaling

(a)

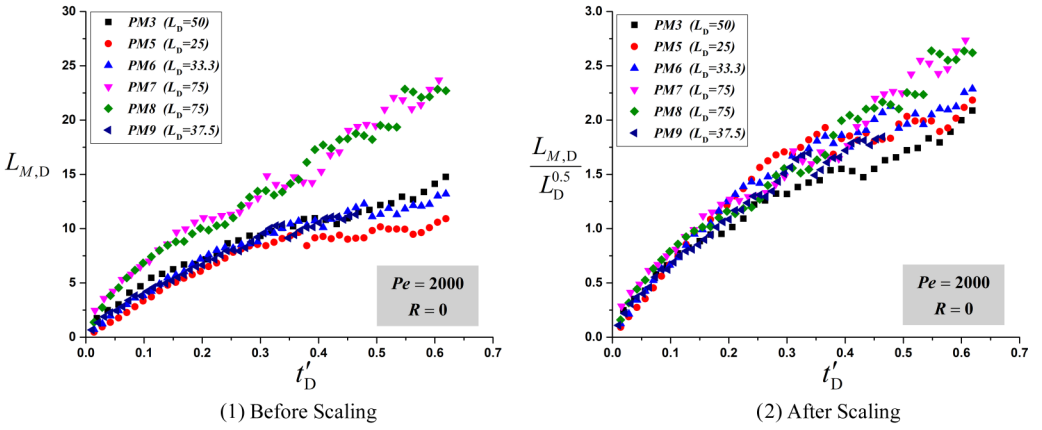

(1) Before Scaling (2) After Scaling

(b)

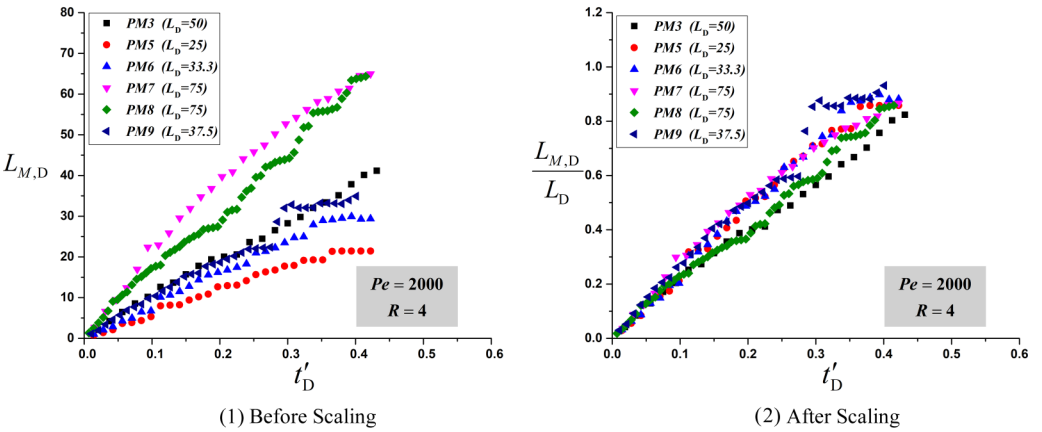

(1) Before Scaling (2) After Scaling

(c)

FIG. 19. Scaling of medium length (L_D) for the mixing length plots of miscible displacements at (a) $R = 0$ and Pe $= 0.2$, (b) $R = 0$ and Pe $= 2000$, and (c) $R = 4$ and Pe $= 2000$. The left-side plots show the variations of mixing length before scaling while the right-side plots correspond to variations after scaling.

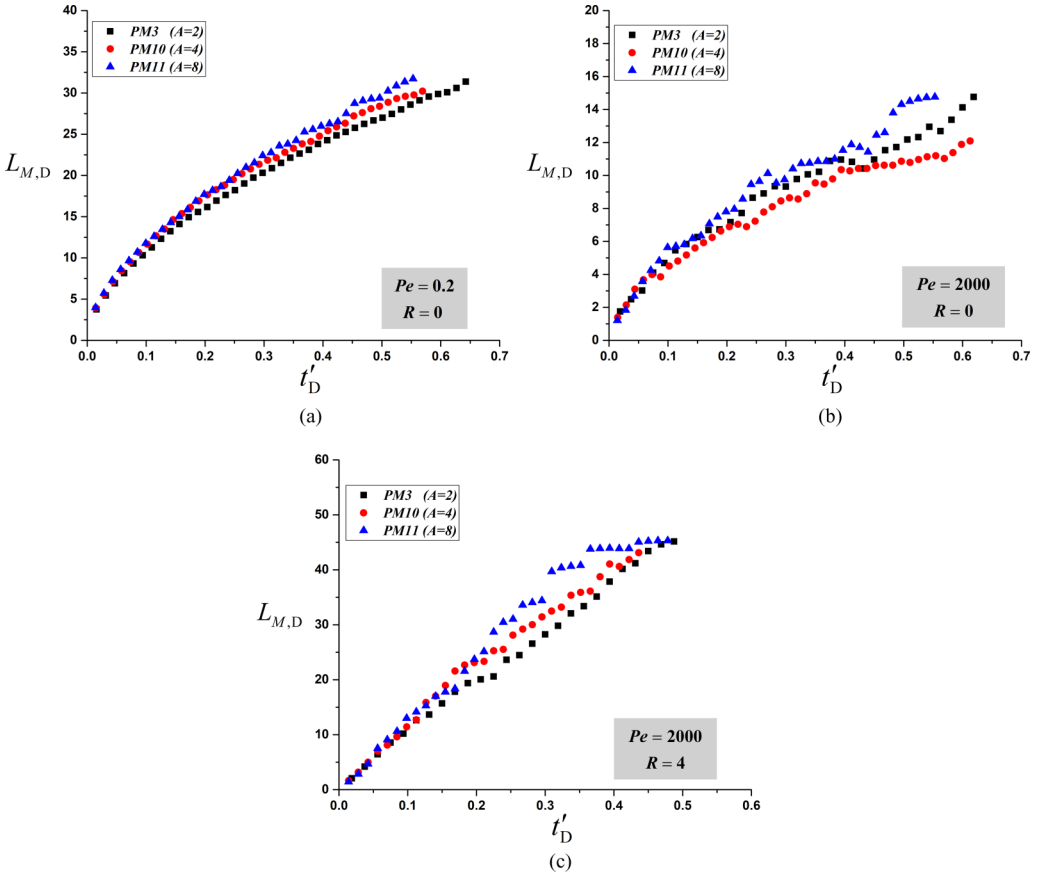

FIG. 20. The effect of aspect ratio (A) on mixing length plots of miscible displacements at (a) $R = 0$ and Pe $= 0.2$, (b) $R = 0$ and Pe $= 2000$, and (c) $R = 4$ and Pe $= 2000$.

APPENDIX

To obtain the distribution of velocity and describe its heterogeneity by the standard deviation of the distribution and the correlation length of velocity variogram, single phase flow simulations are performed on the media PM1 to PM4. Afterwards, the distribution of the magnitude of velocity in the flow direction ($|u_{x,D}|$) is obtained by evaluating the velocity at a set of points covering the whole area of the pattern. Then the standard deviation of these distributions ($S_{|u_{x,D}|}$) are calculated and tabulated in Table II along with CV for each pattern. To define the correlation of velocity fields, the variogram of velocity in the direction of flow are calculated as [45]

$$\gamma_{u_{x,D}}(h_D) = \frac{1}{2}\left[\frac{\sum_{i=1}^{n}[u_{x,D}(x_{i,D}) - u_{x,D}(x_{i,D}+h_D)]^2}{n}\right], \tag{A1}$$

where γ is the variogram, h_D is the lag distance in the x direction, and n is the number of data points in the patterns at which the values of $u_{x,D}$ are evaluated. We also compute the variogram for porosity as [45]

$$\gamma_{\phi}(h_D) = \frac{1}{2}\left[\frac{\sum_{i=1}^{m}[I(x_{i,D}) - I(x_{i,D}+h_D)]^2}{m}\right], \tag{A2}$$

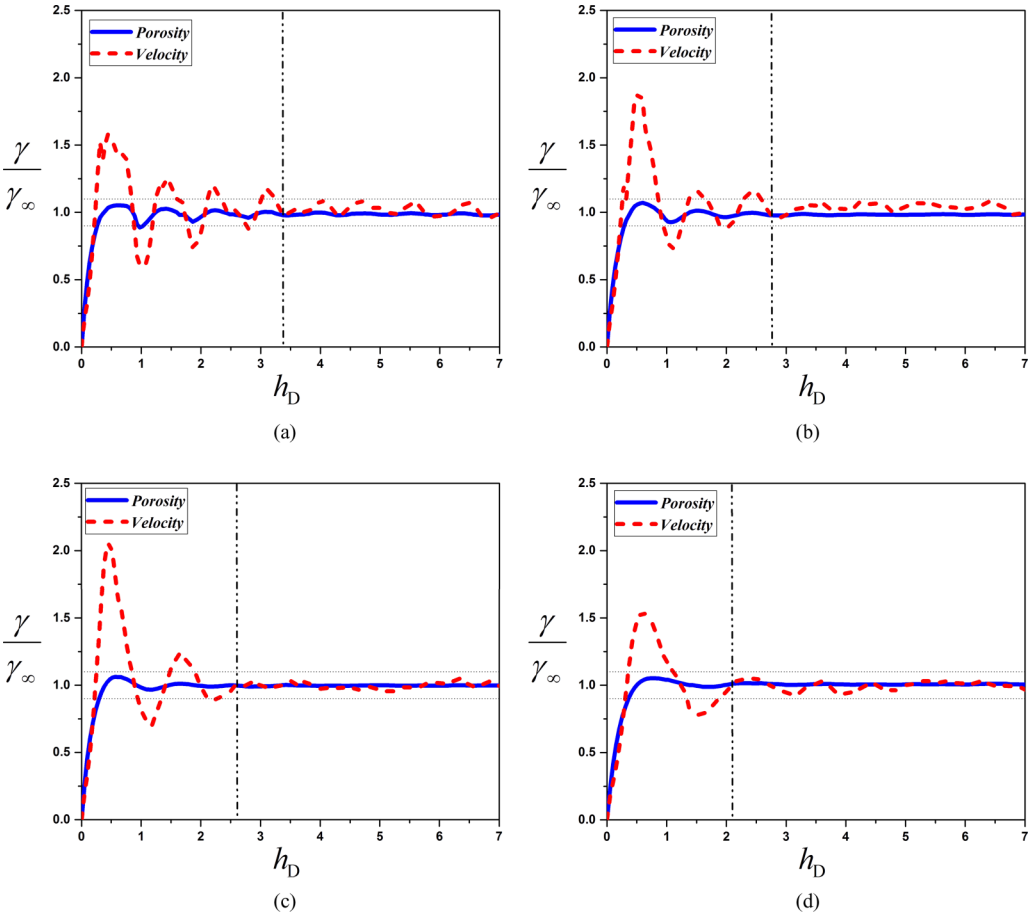

FIG. 21. Normalized variograms of porosity and velocity in the x direction for (a) PM1, (b) PM2, (c) PM3, and (d) PM4. The vertical lines indicate the correlation lengths while the horizontal dash lines represent the range within which the variations of $\gamma/\gamma(\infty)$ assumed to be insignificant.

where I is the indicator function, which equals 1 for the data points on the pore space and 0 for the data points on the grains, and m is the number of data points at which the values of I are obtained. The calculated γ_ϕ and $\gamma_{u_{x,\mathrm{D}}}$ are then normalized by their infinite-range theoretical values of $\gamma_\phi(\infty) = \phi(1-\phi)$ and $\gamma_{u_{x,\mathrm{D}}}(\infty) = \langle {u_{x,\mathrm{D}}}^2 \rangle - \langle u_{x,\mathrm{D}} \rangle^2$, respectively, and plotted in Fig. 21. The correlation lengths (λ_D) of velocity variograms are determined as the values of h_D at which $\gamma/\gamma(\infty)$ approaches 1.0 and remains in the range 1.0 ± 0.1 beyond that. The correlation lengths are indicated by vertical lines in Fig. 21 and presented in Table II.

[1] O. A. Cirpka, G. Chiogna, M. Rolle, and A. Bellin, Transverse mixing in three-dimensional nonstationary anisotropic heterogeneous porous media, Water Resour. Res. **51**, 241 (2015).

[2] C. Nicolaides, B. Jha, L. Cueto-Felgueroso, and R. Juanes, Impact of viscous fingering and permeability heterogeneity on fluid mixing in porous media, Water Resour. Res. **51**, 2634 (2015).

[3] M. Rolle, D. Hochstetler, G. Chiogna, P. K. Kitanidis, and P. Grathwohl, Experimental investigation and pore-scale modeling interpretation of compound-specific transverse dispersion in porous media, Transp. Porous Media **93**, 347 (2012).
[4] M. Rolle and P. K. Kitanidis, Effects of compound-specific dilution on transient transport and solute breakthrough: A pore-scale analysis, Adv. Water Resour. **71**, 186 (2014).
[5] Y. Ye, G. Chiogna, O. Cirpka, P. Grathwohl, and M. Rolle, Experimental investigation of compound-specific dilution of solute plumes in saturated porous media: 2-D vs. 3-D flow-through systems, J. Contam. Hydrol. **172**, 33 (2015).
[6] A. Riaz, M. Hesse, H. A. Tchelepi, and F. M. Orr, Onset of convection in a gravitationally unstable diffusive boundary layer in porous media, J. Fluid Mechan. **548**, 87 (2006).
[7] R. E. Bretz, R. M. Specter, and F. M. Orr Jr., Effect of pore structure on miscible displacement in laboratory cores, SPE Reservoir Eng. **3**, 857 (1988).
[8] L. W. Holm, Miscibility and miscible displacement, J. Petrol. Tech. **38**, 817 (1986).
[9] F. Kamali, F. Hussain, and Y. Cinar, A laboratory and numerical-simulation study of co-optimizing CO_2 storage and CO_2 enhanced oil recovery, Soc. Petrol. Eng. J. **20**, 1227 (2015).
[10] R. J. Blackwell, J. R. Rayne, and W. M. Terry, Factors influencing the efficiency of miscible displacement, Trans. American Institute of Mining, Metallurgical, and Petroleum Engineers (AIME) **217**, 1 (1959).
[11] W. E. Brigham, P. W. Reed, and J. N. Dew, Experiments on mixing during miscible displacement in porous media, Soc. Petrol. Eng. J. **1**, 1 (1961).
[12] A. De Wit and G. M. Homsy, Viscous fingering in periodically heterogeneous porous media. II. Numerical simulations, J. Chem. Phys. **107**, 9619 (1997).
[13] B. Habermann, The efficiency of miscible displacement as a function of mobility ratio, Trans. American Institute of Mining, Metallurgical, and Petroleum Engineers (AIME) **219**, 264 (1960).
[14] S. H. Hejazi and J. Azaiez, Non-linear interactions of dynamic reactive interfaces in porous media, Chem. Eng. Sci. **65**, 938 (2010).
[15] S. H. Hejazi and J. Azaiez, Hydrodynamic instability in the transport of miscible reactive slices through porous media, Phys. Rev. E **81**, 056321 (2010).
[16] S. H. Hejazi and J. Azaiez, Nonlinear simulation of transverse flow interactions with chemically driven convective mixing in porous media, Water Resour. Res. **49**, 4607 (2013).
[17] M. Sajjadi and J. Azaiez, Scaling and unified characterization of flow instabilities in layered heterogeneous porous media, Phys. Rev. E **88**, 033017 (2013).
[18] C. T. Tan and G. M. Homsy, Viscous fingering with permeability heterogeneity, Phys. Fluids A **4**, 1099 (1992).
[19] C. T. Tan and G. M. Homsy, Simulation of nonlinear viscous fingering in miscible displacement, Phys. Fluids **31**, 1330 (1988).
[20] D. U. Von Rosenberg, Mechanics of steady state single-phase fluid displacement from porous media, AIChE J. **2**, 55 (1956).
[21] R. Aris, On the dispersion of a solute in a fluid flowing through a tube, Proc. R. Soc. London A **235**, 67 (1956).
[22] G. Taylor, Dispersion of soluble matter in solvent flowing slowly through a tube, Proc. R. Soc. London A**219**, 186 (1953).
[23] J. R. Waggoner, J. L. Castillo, and L. W. Lake, Simulation of EOR processes in stochastically generated permeable media, SPE Formation Eval. **7**, 173 (1992).
[24] A. Arya, T. A. Hewett, R. G. Larson, and L. W. Lake, Dispersion and reservoir heterogeneity, SPE Reservoir Eng. **3**, 139 (1988).
[25] J. C. Bacri, N. Rakotomalala, D. Salin, and R. Wouméni, Miscible viscous fingering: Experiments versus continuum approach, Phys. Fluids A **4**, 1611 (1992).
[26] J. C. Bacri, D. Salin, and R. Wouméni, Three-Dimensional Miscible Viscous Fingering in Porous Media, Phys. Rev. Lett. **67**, 2005 (1991).
[27] E. J. Peters, R. Gharbi, and N. Afzal, A look at dispersion in porous media through computed tomography imaging, J. Petrol. Sci. Eng. **15**, 23 (1996).

[28] H. A. Tchelepi, F. M. Orr, N. Rakotomalala, D. Salin, and R. Wouméni, Dispersion, permeability heterogeneity, and viscous fingering: Acoustic experimental observations and particle-tracking simulations, Phys. Fluids A **5**, 1558 (1993).
[29] W. B. Zimmerman and G. M. Homsy, Nonlinear viscous fingering in miscible displacement with anisotropic dispersion, Phys. Fluids A **3**, 1859 (1991).
[30] W. B. Zimmerman and G. M. Homsy, Three-dimensional viscous fingering: A numerical study, Phys. Fluids A **4**, 1901 (1992).
[31] L. W. Gelhar and C. L. Axness, Three-dimensional stochastic analysis of macrodispersion in aquifers, Water Resour. Res. **19**, 161 (1983).
[32] L. W. Gelhar, A. L. Gutjahr, and R. L. Naff, Stochastic analysis of macrodispersion in a stratified aquifer, Water Resour. Res. **15**, 1387 (1979).
[33] K. S. Sorbie, F. Feghi, G. E. Pickup, P. S. Ringrose, and J. L. Jensen, Flow regimes in miscible displacements in heterogeneous correlated random fields, SPE Advanced Technol. Series **2**, 78 (1994).
[34] U. G. Araktingi and F. M. Orr Jr., Viscous fingering in heterogeneous porous media, SPE Advanced Technol. Series **1**, 71 (1993).
[35] A. De Wit and G. M. Homsy, Viscous fingering in periodically heterogeneous porous media. I. Formulation and linear instability, J. Chem. Phys. **107**, 9609 (1997).
[36] C. T. Tan and G. M. Homsy, Stability of miscible displacements in porous media: Radial source flow, Phys. Fluids **30**, 1239 (1987).
[37] E. J. Koval, A method for predicting the performance of unstable miscible displacement in heterogeneous media, Soc. Petrol. Eng. J. **3**, 145 (1963).
[38] S. Zheng and D. Yang, Determination of individual diffusion coefficients of C_3H_8/n − C_4H_{10}/CO_2/heavy-oil systems at high pressures and elevated temperatures by dynamic volume analysis, Soc. Petrol. Eng. J. **22**, 0799 (2017).
[39] R. I. Al-Raoush and C. S. Willson, Extraction of physically realistic pore network properties from three-dimensional synchrotron x-ray microtomography images of unconsolidated porous media systems, J. Hydrol. **300**, 44 (2005).
[40] N. R. Morrow, J. D. Huppler, and A. B. Simmons, Porosity and permeability of unconsolidated, upper Miocene sands from grain-size analysis, J. Sediment. Res. **39**, 312 (1969).
[41] *COMSOL Multiphysics User's Guide Version 5.2* (COMSOL Inc., Burlington, MA, 2015).
[42] T. K. Perkins and O. C. Johnston, A review of diffusion and dispersion in porous media, Soc. Petrol. Eng. J. **3**, 70 (1963).
[43] B. Berkowitz and J. Zhou, Reactive solute transport in a single fracture, Water Resour. Res. **32**, 901 (1996).
[44] W. B. Zimmerman and G. M. Homsy, Viscous fingering in miscible displacements: Unification of effects of viscosity contrast, anisotropic dispersion, and velocity dependence of dispersion on nonlinear finger propagation, Phys. Fluids A **4**, 2348 (1992).
[45] B. Bijeljic, A. Raeini, P. Mostaghimi, and M. J. Blunt, Predictions of non-Fickian solute transport in different classes of porous media using direct simulation on pore-scale images, Phys. Rev. E **87**, 013011 (2013).